Determination of the relative orientation between ^{15}N-^{1}H dipolar coupling and ^{1}H chemical shift anisotropy tensors under fast MAS solid-state NMR

Neelam Sehrawat[a,1], Ekta Nehra[a,1], Ketan Kumar Rohilla[a], Takeshi Kobayashi[b], Yusuke Nishiyama[c,d,*], Manoj Kumar Pandey[a,*]

[a] Indian Institute of Technology (IIT) Ropar, Rupnagar, Punjab, 140001, India

[b] U.S. DOE, Ames Laboratory, Iowa State University, Ames, IA, 50011-3020, United States

[c] RIKEN-JEOL Collaboration Center, RIKEN, Yokohama, Kanagawa, 230-0045, Japan

[d] JEOL Ltd., Musashino, Akishima, Tokyo, 196-8558, Japan

* Authors to whom correspondence should be addressed: mkpandey@iitrpr.ac.in, yunishiy@jeol.co.jp

[1] These authors contributed equally to this work

Keywords

Solid-state NMR, CSA, Dipolar coupling, Fast MAS, ROCSA, DIPSHIFT

Abstract

In this work, we have proposed a proton-detected three-dimensional (3D) ^{15}N-^{1}H dipolar coupling (DIP)/^{1}H chemical shift anisotropy (CSA)/^{1}H chemical shift (CS) correlation experiment to measure the relative orientation between the ^{15}N-^{1}H dipolar coupling and the ^{1}H CSA tensors under fast magic angle spinning (MAS) solid-state NMR. In the 3D correlation experiment, the ^{15}N-^{1}H dipolar coupling and ^{1}H CSA tensors are recoupled using our recently developed windowless *C*-symmetry-based $C3_3^1$-ROCSA (recoupling of chemical shift anisotropy) DIPSHIFT and $C3_3^1$ -ROCSA pulse-based methods, respectively. The 2D ^{15}N-^{1}H DIP/^{1}H CSA powder lineshapes extracted using the proposed 3D correlation method are shown to be sensitive to the sign and asymmetry of the ^{1}H CSA tensor, a feature that allows the determination of the relative orientation between the two correlating tensors with improved accuracy. The experimental method developed in this study is demonstrated on a powdered U-^{15}N L-Histidine.HCl.H_2O sample.

Introduction

Nuclear spin interactions characterized by nuclear magnetic resonance (NMR) spectroscopy carry a wealth of information in terms of electronic/molecular environment, internuclear distances, relative orientations, etc., for chemical, materials, and biological systems at an atomic level [1]. In particular, knowledge about the relative orientation between the nuclear spin interactions is essential for structural characterization [2–8]. Unlike solution samples, restricted mobility of molecules in solids results in un-averaged orientation-dependent/anisotropic nuclear spin interactions like chemical shift anisotropy (CSA), dipolar and quadrupolar couplings. Consequently, solid-state NMR (ssNMR) spectra of powdered solids, in general, are broad/featureless, and magic angle spinning (MAS) [9,10] in combination with the radio-frequency (rf) pulses [1,11–13] is employed to achieve averaging in spatial and spin spaces, respectively. Subsequently, a better site resolution and improved sensitivity of a ssNMR spectrum are accomplished but only at the cost of structural constraints. To regain information on these constraints, a host of recoupling experiments are designed and developed to recouple anisotropic interactions of choice under MAS [14–24]. In the past, the design of the ^{1}H CSA and ^{15}N-^{1}H dipolar coupling recoupling-based experimental methods at fast MAS rates has enjoyed considerable popularity [25–36]. While the ^{1}H CSA plays an important role in providing structural information in terms of electrostatic, inter/intramolecular hydrogen bonding, and π-electrons interactions [37–40], heteronuclear dipolar couplings (X-^{1}H) are used for distance measurements. Particularly, nitrogen-connected protons (NH) in chemical and biological solids provide structural stability through hydrogen bonding interactions and are sensitive to the local electronic environment and dynamics. Nevertheless, the measurement of the ^{1}H CSA has majorly been challenging due to the small ^{1}H chemical shift distribution and homogeneously broadened lineshapes emerging from the presence of strong ^{1}H-^{1}H homonuclear dipolar interactions [41]. However, the advent of fast MAS probe technology that provides enhanced resolution and sensitivity in proton-based measurements has now enabled the determination of the ^{1}H CSA with ease [42–46]. Unlike slow MAS studies, the role of fast MAS is to average out homonuclear dipolar interactions to an extent that the ^{1}H CSA can be measured in the absence of ^{1}H-^{1}H homonuclear decoupling required during the data acquisition. In the past, we presented a

γ-encoded *R*-symmetry-based 2D ^{1}H CSA/^{1}H CS recoupling method at fast MAS, which is less sensitive to the presence of rf field inhomogeneity and resulted in a good CSA recoupling efficiency [43,44] but only at the cost of sign of the CSA due to elimination of the $|m| = 1$ spatial component of the ^{1}H CSA tensor. Indeed, a simultaneous recoupling of the $|m| = 1$ and $|m| = 2$ spatial components of the CSA tensor is essential for the determination of the sign of the CSA. Recently, a windowless *C*-symmetry-based recoupling of CSA (ROCSA) sequence [42,47] was proposed enabling the determination of magnitude, sign and asymmetry parameter (η) of the ^{1}H CSA with suppression of ^{1}H-^{1}H homonuclear dipolar interactions in the first-order average Hamiltonian [42]. Later, the windowless ROCSA sequence was integrated with the DIPSHIFT pulse-based method for the measurement of NH distances in biological solids wherein recoupling of the ^{15}N-^{1}H dipolar couplings was accomplished and one-bond (short) NH distances were reported [48]. The windowless ROCSA-based DIPSHIFT method was shown to be immune to the ^{1}H CSA under ^{15}N evolution and to the ^{1}H-^{1}H homonuclear dipolar interactions up to the first-order average Hamiltonian. While information about the ^{1}H CSA (magnitude, sign and asymmetry) and NH dipolar coupling strengths is essential for the structural characterization of solids, particularly knowledge about the relative orientation [49–58] between the NH dipolar coupling vector and the principal axis system (PAS) of the ^{1}H (^{15}N) CSA tensor provides better insights for structural refinement and validation. In this report, we have integrated the above two methods and developed a proton-detected 3D ^{15}N-^{1}H dipolar coupling/^{1}H CSA/^{1}H CS (^{15}N-^{1}H DIP/^{1}H CSA/^{1}H CS) correlation experiment to measure the relative orientation between ^{15}N-^{1}H dipolar coupling and ^{1}H CSA tensors at a fast MAS rate of 69.832 kHz. The feasibility of our proposed method is demonstrated on a powdered U-^{15}N labeled L-Histidine.HCl.H_2O sample.

Pulse sequence

The proton-detected 3D ^{15}N-^{1}H DIP/^{1}H CSA/^{1}H CS pulse sequence developed in the present study for the measurement of the relative orientation between ^{15}N-^{1}H DIP and ^{1}H CSA tensors is shown in **Figure 1**. The ^{1}H transverse magnetization is first created with the application of an initial 90° pulse on the ^{1}H channel. A ramped amplitude modulated

cross-polarization (RAMP-CP) step is used to transfer the ^{1}H magnetization to ^{15}N [59]. Following the first CP step, the ROCSA DIPSHIFT block is implemented to measure ^{15}N-^{1}H dipolar couplings. The ^{15}N transverse magnetization evolves for constant echo duration, *T*. In order to refocus the ^{15}N isotropic chemical shifts, a 180° pulse is inserted in the middle of the duration *T*. The ^{15}N-^{1}H dipolar couplings are expressed during the incremental t_1 duration through the application of a rotor-synchronized windowless *C*-symmetry-based [60] ROCSA pulse sequence $C3_3^1\left(90_0360_{180}270_0270_0360_{180}90_0\right)$ [42] on the ^{1}H channel, henceforth referred to as the windowless $C3_3^1$-ROCSA-DIPSHIFT for recoupling of NH dipolar coupling. The scaling factor for the windowless ROCSA pulse sequence is 0.246 [42]. A low-power heteronuclear continuous-wave (CW) decoupling on the ^{1}H channel is applied for a duration T-t_1 following the windowless $C3_3^1$-ROCSA. The role of the constant time procedure is to eliminate the signal modulations due to the ^{15}N CSA, ^{15}N-^{15}N dipolar and *J*-coupling interactions during the ^{15}N-^{1}H DIP recoupling duration. Moreover, simultaneously recoupled ^{1}H CSA during the windowless ROCSA duration does not interfere with the ^{15}N-^{1}H dipolar couplings under the ^{15}N evolution in the first-order average Hamiltonian [11,61], a feature that is essential for getting undistorted NH DIP powder lineshapes. The above observation under the ^{15}N evolution is due to the presence of a commuting set of recoupled ^{1}H CSA (I_z) and ^{15}N-^{1}H DIP (I_zS_z) operators in the first-order average Hamiltonian. The ^{15}N magnetization is stored along the z-direction by the application of a 90° pulse after the constant time duration *T*. The unwanted transverse ^{1}H magnetization is suppressed by the application of phase-alternated (xyxy) purge pulses that serves as an alternative to the HORROR irradiation on the ^{1}H channel. The advantage of being at a long-duration irradiation with an application of weaker ^{1}H rf amplitude is to avoid any sample heating and/or hardware failure. A 90° pulse on the ^{15}N channel restores the ^{15}N transverse magnetization for the second ^{15}N-^{1}H RAMP-CP transfer step. The ^{1}H magnetization is allowed to evolve in the presence of the recoupled ^{1}H CSA by implementing the windowless $C3_3^1$-ROCSA during the incremental t_2 duration. A 180° pulse on the ^{15}N channel is applied in the middle of the ^{1}H CSA recoupling duration to decouple the ^{15}N-^{1}H heteronuclear couplings which are also reintroduced by the windowless $C3_3^1$-ROCSA. The ^{1}H transverse magnetization is

restored to the z-direction for a short duration t_z (z-filter) for getting rid of any residual transversal ^{1}H magnetization, and to ensure symmetry coherence selection pathway in the t_2 dimension for the quadrature detection. Finally, a 90° read pulse is applied on the proton channel under the ^{15}N-^{1}H WALTZ decoupling, which is applied on the ^{15}N channel during the acquisition duration, t_3. Rotor-synchronization was activated after the application of the initial ^{1}H 90° pulse to avoid the loss of phase coherence between the rotor and applied recoupling blocks.

Experimental

All the NMR data were collected on a JEOL spectrometer (Model: JNM-ECZ600R, JEOL RESONANCE Inc., Japan) operating at ^{1}H and ^{15}N Larmor frequencies of 599.672 and 60.764 MHz, respectively. Approximately 1.0 mg (0.8 μL) of powdered U-^{15}N L-Histidine.HCl.H_2O (U-^{15}N L-His.HCl.H_2O) was packed into a 1.0 mm zirconia rotor. Sample spinning was carried out at a fast MAS rate (ν_r) of 69.832 kHz in a 1.0 mm double-resonance (HX) fast MAS probe (JEOL RESONANCE Inc., Japan) at an ambient temperature. A recycle delay of 7 s was used in the proton-detected 3D ^{15}N-^{1}H DIP/^{1}H CSA/^{1}H CS correlation experiment. The 90° pulse lengths were calibrated to 0.84 and 1.94 μs for ^{1}H and ^{15}N, respectively. In order to avoid sample heating due to strong rf fields, double-quantum (DQ) Hartmann-Hahn CP matching conditions [62] (~19 kHz and 48 kHz on the ^{1}H and ^{15}N channels, respectively) under MAS were used for all the RAMP-CP steps. While a longer contact time of 2 ms during the first CP step was used to maximize the ^{1}H to ^{15}N CP magnetization transfer efficiency, a shorter contact time of 0.3 ms was used in the second CP step for the ^{15}N to ^{1}H magnetization transfer to select directly bonded NH proton resonances. The absence of ^{1}H-^{1}H spin diffusion during the second CP contact time of 0.3 ms was confirmed by the absence of any long-range or remote ^{15}N/^{1}H isotropic chemical shift correlations in the proton-detected 2D ^{15}N CS/^{1}H CS correlation experiment (Refer to **Figure S10** in the Supporting Information). To decouple heteronuclear (^{15}N-^{1}H) dipolar interactions, a WALTZ decoupling of strength ~ 9.4 kHz during the duration T-t_1 on the ^{1}H channel and a WALTZ decoupling with a strength of ~ 7 kHz during the ^{1}H acquisition period ($t_{3,\ max}$ = 8.192 ms) on the ^{15}N channel were applied. The constant spin echo-time duration T was set as per the

expression: $T = 2\tau_r \times ((t_1 \text{ increments} \times 3) + 1)$; here, τ_r is the rotor period [48]. Prior to the 90° read pulse, a z-filter (t_z) with a duration of 1 ms was implemented to remove any residual transversal ^{1}H magnetization. Phase-alternated purge pulses were applied for 200 ms with the ^{1}H rf field amplitude of 9.4 kHz. As demonstrated previously [63] the ^{15}N/^{15}N spin diffusion process during this duration is expected to be negligible due to weaker ^{15}N-^{15}N homonuclear dipolar coupling. The ^{15}N-^{1}H heteronuclear dipolar couplings (using windowless $C3_3^1$ -ROCSA-DIPSHIFT) and the ^{1}H CSA (using windowless $C3_3^1$-ROCSA) were recoupled during 16 t_1 and 16 t_2 incremental evolution periods, respectively. Recoupled signals were obtained at every $6\tau_r$ with a rf field strength of $4\nu_r N/n$ = 279.3 kHz. For each t_1 and t_2 time point increment, 16 scans were collected (total experimental time: 15.9 hours). The States-TPPI method in the ^{1}H CSA dimension was applied to obtain the phase-sensitive recoupled signal, while only magnitude was observed in the DIPSHIFT dimension. Delta NMR software (JEOL RESONANCE Inc.) was used to process all the NMR experimental data. The ^{15}N-^{1}H DIP and ^{1}H CSA recoupling dimensions were processed using zero filling with twelve times the data size before the Fourier transform (FT). SIMPSON software [64,65] was used to simulate the recoupled ^{15}N-^{1}H DIP and ^{1}H CSA powder lineshapes using REPULSION-678 (α, β) crystallite orientations and 60 γ-angles [66]. The 2D ^{15}N-^{1}H DIP/^{1}H CSA powder spectra were simulated using REPULSION-168 (α, β) crystallite orientations and 60 γ-angles. The principal components of ^{1}H chemical shift tensors are represented as δ_{xx}, δ_{yy} and δ_{zz} and are described using the Haeberlen convention [1]. The expressions $\delta_{iso} = (\delta_{xx}+\delta_{yy}+\delta_{zz})/3$, $\delta_{ani} = \delta_{zz} - \delta_{iso}$, and $\eta = (\delta_{yy} - \delta_{xx})/\delta_{ani}$, represent the isotropic chemical shift, CSA and asymmetry parameters, respectively.

Results and Discussion

The experimental method developed in this work involves a correlation between ^{15}N-^{1}H DIP and ^{1}H CSA interactions to obtain one of the essential structural constraints, namely, the relative orientation between the two tensors. For demonstrating the concept and highlighting the benefits of the proposed windowless $C3_3^1$-ROCSA-based approach over existing γ-encoded R-symmetry-based sequences, we first carried out a careful

investigation of a series of 2D ^{15}N-^{1}H DIP/^{1}H CSA powder lineshapes generated with a variation of ^{1}H CSA and ^{15}N-^{1}H DIP parameters using the SIMPSON software. As the recoupled time domain signals obtained from the γ-encoded *R*-symmetry-based sequences are amplitude modulated, no information is rendered on the sign of the ^{1}H CSA. The real Fourier transform of the amplitude-modulated signal leads to a mirror-symmetric ^{1}H CSA powder pattern. In such a scenario, the available spectral area resulting from the 2D powder pattern for numerical data fitting is reduced by a factor of four in contrast to half using the proposed windowless ROCSA-based approach for the ^{15}N-^{1}H DIP (axially symmetric pseudo Pake-doublet powder pattern) and ^{1}H CSA correlation. This aspect is demonstrated through numerical simulations carried out with a variation of the ^{15}N-^{1}H DIP principal axis system (PAS) angles (α_{d}, β_{d}, γ_{d}) while keeping the ^{1}H CSA PAS angles (α_{CSA}, β_{CSA}, γ_{CSA}) fixed to zero. In this representation, β_{d} and γ_{d} correspond to the angles between the *z*-component of the CSA tensor (δ_{zz}) and the dipolar vector, and the *x*-component of the CSA tensor (δ_{xx}) and the projection of the dipolar vector onto the *xy*-plane of the CSA tensor, respectively. In other words, the two-angle set (β_{d} and γ_{d}) represents the polar and azimuthal angles of the dipolar-coupling vector in the PAS of CSA as shown in **Figure 2**. Since β_{d} is the angle with respect to the δ_{zz} component of the ^{1}H chemical shift tensor, any variation in this angle is expected to alter the shape of the 2D ^{15}N-^{1}H DIP/^{1}H CSA powder spectrum significantly. As depicted in **Figure 3**, a definite change in the shape of the simulated 2D ^{15}N-^{1}H DIP/^{1}H CSA powder lineshapes is observed with a variation in the β_{d} angles for a fixed ^{1}H CSA parameters and the ^{15}N (*S*)-^{1}H (*I*) DIP constant ($D_{IS} = b_{IS}/2\pi = -\mu_0\gamma_I\gamma_S\hbar/8\pi^2 r_{IS}^3$ = 9.6 kHz), both from the proposed windowless $C3_3^1$-ROCSA and γ-encoded $R18_8^7(270^\circ 90^\circ)$-symmetry-based correlation methods. However, the availability of a larger spectral area originating from the sign discrimination of the ^{1}H CSA from the ROCSA-based method in the 2D ^{15}N-^{1}H DIP/^{1}H CSA powder lineshapes (**Figure 3** (A1)-(A5): δ_{ani} = 15.8 ppm, η = 0.5; **Figure 3** (B1)-(B5): δ_{ani} = -15.8 ppm, η = 0.5) is clearly visible unlike the mirror-symmetric (sign insensitive) ^{1}H CSA lineshapes from the γ-encoded *R*-symmetry-based pulse sequence (**Figure 3** (C1)-(C5): δ_{ani} = +/-15.8 ppm, η = 0.5). This feature is beneficial for the determination of the relative orientation between the two correlating tensors with improved accuracy. Moreover, a noticeable change in the shape of the 2D

^{15}N-^{1}H DIP/^{1}H CSA powder lineshapes is also observed with respect to the γ_d angle variation in the windowless ROCSA-based approach unlike in the γ-encoded *R*-symmetry-based sequence (**Figure 4**). This feature again is unique to our proposed method for the determination of the relative orientation between the correlating tensors. It is noteworthy that the shape of the 2D ^{15}N-^{1}H DIP/^{1}H CSA powder lineshapes is independent of γ_d angle for β_d values less than 30°. As expected, the 2D ^{15}N-^{1}H DIP/^{1}H CSA powder pattern remains mostly invariant with the variation in α_d DIP PAS angles (data not shown) due to an axially symmetric DIP tensor. Notably, the 2D ^{15}N-^{1}H DIP/^{1}H CSA powder pattern repeats itself with a minor deviation for the β_d and 180°− β_d or γ_d and 180°− γ_d pairs from the proposed method (**Figures 7-8,** and **Figures S5, S6 and S8** in the supporting information)**.** If (0°, β_d, γ_d) represents the relative orientation between the ^{15}N-^{1}H DIP and ^{1}H CSA tensors then so as (0°, 180° − β_d, γ_d), (0°, β_d, 180°− γ_d) and (0°, 180° − β_d, 180° − γ_d). Previously, the windowless ROCSA-based method was shown to be more sensitive towards the variation of the asymmetry (η) of the ^{1}H CSA in comparison to the γ-encoded *R*-symmetry-based methods [42]. Therefore, the shape of the 2D ^{15}N-^{1}H DIP/^{1}H CSA powder pattern from the windowless ROCSA-based method is expected to change considerably with the variation of η. This aspect is highlighted through the numerical simulations from the two methods wherein the ^{15}N-^{1}H DIP/^{1}H CSA powder lineshapes are generated with a variation of the η at a fixed β_d angle (30°), and a constant magnitude of ^{1}H CSA (15.8 ppm) and the ^{15}N-^{1}H DIP constant (9.6 kHz) (**Figure 5**). It is evident that the shape of the 2D ^{15}N-^{1}H DIP/^{1}H CSA powder lineshape is more sensitive towards a variation in the asymmetry of the ^{1}H CSA from the windowless ROCSA-based method as compared to the γ-encoded *R*-symmetry -based method. The 1D projections on the ^{1}H CSA dimension (**Figure S1** of the supporting information) of the simulated 2D ^{15}N-^{1}H DIP/^{1}H CSA spectra with the η variation from the two methods shown in **Figure 5** can also be used to bring more clarity on this aspect. It should be noted that the absence of mirror symmetry in the CSA powder lineshape using the windowless ROCSA-based approach will be highly advantageous for the CSA/CSA correlation experiments [50] as it means that a full

2D spectral area/powder lineshape will be available for numerical data fitting, hence leading to a unique determination of the relative orientation.

Using the pulse sequence shown in **Figure 1**, the 3D ^{15}N-^{1}H DIP/^{1}H CSA/^{1}H CS correlation experiment was conducted. For the determination of the ^{15}N-^{1}H dipolar coupling strengths and ^{1}H CSA (sign and magnitude, and η), the 2D planes of ^{15}N-^{1}H DIP/^{1}H CS and ^{1}H CSA/^{1}H CS, respectively, were extracted from the 3D correlation spectrum of U-^{15}N L-His.HCl.H_2O (**Figure S2** of the supporting information**)**. The dipolar coupling strengths obtained from the best-fitted ^{15}N-^{1}H dipolar powder lineshape are 9.5 kHz and 10.1 kHz, with an error in the range of ca. ± 0.5 kHz for the N(1)H and N(2)H groups present in the imidazole ring of U-^{15}N L-His.HCl.H_2O, respectively (**Figure S3** of the supporting information). The ^{15}N-^{1}H dipolar couplings are converted to NH distances as 1.09 Å and 1.06 Å for N(1)H and N(2)H groups, respectively, and are in good agreement with the results reported in the literature [48,67–69]. Best-fitted ^{1}H CSA powder lineshapes resulted in δ_{ani} = -15.3 ± 1.0 ppm, η = 0.35 ± 0.1 and δ_{ani} = -7.8 ± 1.0 ppm, η = 0.9 ± 0.1) for N(1)H and N(2)H groups of U-^{15}N L-His.HCl.H_2O, respectively, (**Figure S4** of the supporting information), and corroborates well with the literature values [45]. Due to the associated larger ^{1}H CSA asymmetry parameter for N(2)H group, the determination of sign from the numerical simulation was difficult. We have considered negative sign as per the results from density functional theory (DFT)-based quantum chemical calculations. Quantum chemical calculation details can be found in the supporting information. For the determination of the relative orientation between the ^{15}N-^{1}H DIP and the ^{1}H CSA tensors associated with the imidazole ring NH groups of U-^{15}N L-His.HCl.H_2O, the 2D ^{15}N-^{1}H DIP/^{1}H CSA planes were extracted from the 3D ^{15}N-^{1}H DIP/^{1}H CSA/^{1}H CS correlation spectrum at the isotropic ^{1}H chemical shifts of the N(1)H (**Figure 6 A1**) and N(2)H (**Figure 6 A2**) groups. Numerical simulations were carried out to get the best fit of the 2D ^{15}N-^{1}H DIP/^{1}H CSA powder spectra. With a prior knowledge of the ^{15}N-^{1}H dipolar coupling strength and ^{1}H CSA parameters (magnitude, sign and asymmetry parameter) extracted from their respective 2D planes of the 3D ^{15}N-^{1}H DIP/^{1}H CSA/^{1}H CS correlation data, the 2D ^{15}N-^{1}H DIP/^{1}H CSA powder spectra from the experiment were fitted by varying the ^{15}N-^{1}H DIP principal axis system (PAS) angles (β_d and γ_d) while keeping the ^{1}H CSA PAS angles (α_{CSA}, β_{CSA}, γ_{CSA}) fixed to zero. The

right panel of **Figure 6** depicts the best-fitted 2D ^{15}N-^{1}H DIP/^{1}H CSA powder spectra of imidazole N(1)H (**Figure 6 B1**) and N(2)H (**Figure 6 B2**) groups in U-^{15}N L-His.HCl.H_2O with relative orientations (0°, 6°/174°, 0°) and (0°, 8°/172°, 0°) with respect to the ^{1}H CSA tensors, respectively, within an error limit of ± 5°. The above values were obtained after a series of numerical simulations carried out with a variation of the ^{15}N-^{1}H DIP PAS angles (β_d and γ_d). Firstly numerical simulations were carried out with a variation of β_d from 0° to 180° in the step size of 10° using the ^{15}N-^{1}H DIP constant (9.5 kHz) and ^{1}H CSA parameters (δ_{ani} = -15.3 ppm, η = 0.35) corresponding to the N(1)H group of U-^{15}N L-His.HCl.H_2O (**Figure 7**). As expected and also discussed above through numerical simulations, the 2D powder lineshapes change significantly with every 10°-20° change in the β_d angle from the proposed method. However the simulated 2D powder lineshapes for angles $0° \leq \beta_d \leq 20°$ for N(1)H group resemble more closely with the experimental 2D powder lineshapes. In order to further refine the 2D ^{15}N-^{1}H DIP/^{1}H CSA spectral fitting, we carried out numerical simulations with a finer step size of β_d (= 1°) for angles $0° \leq \beta_d \leq 20°$ for N(1)H group (**Figure S7 of the supporting information**). A careful inspection of the 2D ^{15}N-^{1}H DIP/^{1}H CSA spectral features with β_d = 6°/174° ± 5° resembled close to the experimental powder pattern. A similar exercise was repeated to get the best-fitted 2D ^{15}N-^{1}H DIP/^{1}H CSA powder spectrum for the N(2)H group of U-^{15}N L-His.HCl.H_2O and the β_d between the ^{15}N-^{1}H DIP and ^{1}H CSA was found to be 8°/172° ± 5° (see **Figures S8 and S9** of the supporting information). Since β_d is found to be less than 15° for both NH groups, any variation in the γ_d angles has negligible effect on the 2D ^{15}N-^{1}H DIP/^{1}H CSA powder lineshapes (**Figure 8**). The experimental β_d values obtained are found to be in a good agreement with the density functional theory (DFT)-based quantum chemical calculations (6.4° and 12° for the N(1)H and N(2)H, respectively). The error bar reported in this work is based on our conclusion from the manual powder lineshape fitting in the absence of any software-based iterative lineshape-fitting tool. All numerical simulations were carried out in a model two-spin framework; minor contributions from the long-range/remote ^{15}N-^{1}H dipolar couplings to the experimental 2D ^{15}N-^{1}H DIP/^{1}H CSA powder spectra cannot be ruled out. Moreover, different orientation selections during the CP and CSA recoupling steps may also contribute to the error in the relative orientation values. Continuous-wave CP for

polarization transfer during the second CP in the simulation program in contrast to the ramp-CP step used in the experiment may also contribute to error in the reported relative orientation values. Though manual-fitting procedure may be adopted for the determination of the relative orientation between the tensors in systems with a fewer correlating sites, development of an auto-fitting program tool for extracting the best-fit relative orientation values will be essential for systems having a large number of correlating sites with reduced human effort and errors [64,65,70].

Conclusions

In summary, we have designed a proton-detected 3D ^{15}N-^{1}H DIP/^{1}H CSA/^{1}H CS correlation experiment under fast MAS to determine the relative orientation between the ^{15}N-^{1}H DIP and ^{1}H CSA tensors of the nitrogen-bound imidazole group protons of powdered U-^{15}N L-His.HCl.H_2O sample. In the proposed pulse sequence, we have integrated the windowless *C*-symmetry-based $C3_3^1$ -ROCSA-DIPSHIFT and $C3_3^1$ -ROCSA methods for the reintroduction of the ^{15}N-^{1}H DIP and ^{1}H CSA, respectively. Unlike the existing γ-encoded *R*-symmetry-based methods for the relative orientation measurements, the 2D ^{15}N-^{1}H DIP/^{1}H CSA powder lineshapes extracted using the proposed method are sensitive to the sign of the ^{1}H CSA and therefore, allows a larger spectral area for the data fitting. Moreover, the shape of the 2D ^{15}N-^{1}H DIP/^{1}H CSA powder pattern exhibits profound dependence on the asymmetry of the ^{1}H CSA, and DIP PAS angles (β_d and γ_d) in the windowless ROCSA-based approach in comparison to the γ-encoded *R*-symmetry-based method. All such features are beneficial for the determination of the relative orientation between the two correlating tensors with improved accuracy. We believe our study can be extended to the larger chemical and biological systems for their structural refinement and validation.

Data availability

Experimental data will be made available on request.

Declaration of Competing Interest

The authors declare that they have no known competing financial interests or personal relationships that could have appeared to influence the work reported in this paper.

Acknowledgements

M.K.P. would like to acknowledge the Science and Engineering Research Board (SERB)-Department of Science and Technology (DST), Government of India (SERB DST Grant ECR/2017/000713) and IIT Ropar for the financial support. N.S. and E.N. would like to acknowledge IIT Ropar for the graduate assistantship. K.K.R. acknowledges the financial support from the University Grants Commission (UGC), Government of India. This work was supported by JSPS KAKENHI Grant Number 20K05483 and in part, by the JST-Mirai Program (Grant No. JPMJMI17A2, Japan) to Y.N. This work was supported by the U.S. Department of Energy (DOE), Office of Science, Basic Energy Sciences, Materials Science and Engineering Division to T.K. The Ames Laboratory is operated for the DOE by Iowa State University under contract No. DE-AC02-07CH11358 (TK).

References

[1] U. Haeberlen, High resolution NMR in solids, Academic Press, New York, 1976.

[2] K. Takegoshi, T. Imaizumi, T. Terao, One- and two-dimensional ^{13}C–^{1}H/^{15}N–^{1}H dipolar correlation experiments under fast magic-angle spinning for determining the peptide dihedral angle φ, Solid State Nucl. Magn. Reson. 16 (2000) 271–278. https://doi.org/10.1016/S0926-2040(00)00076-X.

[3] R.D. O'Connor, J. Schaefer, Relative CSA-dipolar orientation from REDOR sidebands, J. Magn. Reson. 154 (2002) 46–52. https://doi.org/10.1006/jmre.2001.2461.

[4] B.W. Wilson, A.A. Parker, T. Gullion, Determining the relative orientation between the chemical shift anisotropy and heteronuclear dipolar tensors in static solids by SEDOR NMR, Solid State Nucl. Magn. Reson. 79 (2016) 1–5. https://doi.org/10.1016/j.ssnmr.2016.09.001.

[5] F.G. Vogt, J.M. Gibson, S.M. Mattingly, K.T. Mueller, Determination of molecular geometry in solid-state NMR: Rotational-echo double resonance of three-spin systems, J. Phys. Chem. B. 107 (2003) 1272–1283. https://doi.org/10.1021/jp021686f.

[6] L.B. Andreas, A.K. Mehta, M.A. Mehta, Determination of global structure from distance and orientation constraints in biological solids using solid-state NMR spectroscopy, J. Am. Chem. Soc. 129 (2007) 15233–15239. https://doi.org/10.1021/ja074789q.

[7] M.G. Munowitz, R.G. Griffin, G. Bodenhausen, T.H. Huang, Two-dimensional rotational spin-echo nuclear magnetic resonance in solids: correlation of chemical shift and dipolar interactions, J. Am. Chem. Soc. 103 (1981) 2529–2533. https:// doi.org/10.1021/ja00400a007.
[8] J. Leppert, B. Heise, R. Ramachandran, ^{15}N Chemical shift tensor magnitude and orientation in the molecular frame of uracil determined via MAS NMR, J. Magn. Reson. 145 (2000) 307–314. https://doi.org/10.1006/jmre.2000.2087.
[9] E.R. Andrew, A. Bradbury, R.G. Eades, Removal of dipolar broadening of nuclear magnetic resonance spectra of solids by specimen rotation, Nature. 183 (1959) 1802–1803. https://doi.org/10.1038/1831802a0.
[10] I.J. Lowe, Free induction decays of rotating solids, Phys. Rev. Lett. 2 (1959) 285–287. https://doi.org/10.1103/PhysRevLett.2.285.
[11] U. Haeberlen, J.S. Waugh, Coherent averaging effects in magnetic resonance, Phys. Rev. 175 (1968) 453–467. https://doi.org/10.1103/PhysRev.175.453.
[12] M. Mehring, High resolution NMR spectroscopy in solids, Springer-Verlag Berlin, Heidelberg, 1976.
[13] C.P. Slichter, Principles of magnetic resonance, 3rd ed., Springer-Verlag Berlin, Heidelberg, 1996.
[14] A.E. Bennett, C.M. Rienstra, J.M. Griffiths, W. Zhen, P.T. Lansbury Jr., R.G. Griffin, Homonuclear radio frequency-driven recoupling in rotating solids, J. Chem. Phys. 108 (1998) 9463–9479. https://doi.org/10.1063/1.476420.
[15] J.D. Gross, D.E. Warschawski, R.G. Griffin, Dipolar recoupling in MAS NMR: a probe for segmental order in lipid bilayers, J. Am. Chem. Soc. 119 (1997) 796–802. https://doi.org/10.1021/ja962951b.
[16] R.G. Griffin, Dipolar recoupling in MAS spectra of biological solids, Nat. Struct. Biol. 5 (1998) 508–512. https://doi.org/10.1038/749.
[17] M.H. Levitt, T.G. Oas, R.G. Griffin, Rotary resonance recoupling in heteronuclear spin pair systems, Isr. J. Chem. 28 (1988) 271–282. https://doi.org/10.1002/ ijch.198800039.
[18] G. de Pape, Dipolar recoupling in magic angle spinning solid-state nuclear magnetic resonance, Annu. Rev. Phys. Chem. 63 (2012) 661–684. https://doi.org/10.1146/annurev-physchem-032511-143726.
[19] S.O. Smith, Magic angle spinning NMR methods for internuclear distance measurements, Curr. Opin. Struct. Biol. 3 (1993) 755–759. https://doi.org/ 10.1016/0959-440X(93)90060-X.
[20] U. Sivaranjan, R. Ramachandran, Unraveling multi-spin effects in rotational resonance nuclear magnetic resonance using effective reduced density matrix theory, J. Chem. Phys. 140 (2014) 054101--10. https://doi.org/10.1063/1.4863212.
[21] M. Baldus, D.G. Geurts, B.H. Meier, Broadband dipolar recoupling in rotating solids: a numerical comparison of some pulse schemes, Solid State Nucl. Magn. Reson. 11 (1998) 157–168. https://doi.org/10.1016/S0926-2040(98)00036-8.

[22] S. Dusold, A. Sebald, Dipolar recoupling under magic-angle spinning conditions, Annu. Rep. NMR Spectrosc. 41 (2000) 185–264. https://doi.org/10.1016/s0066- 4103(00)41010-0.
[23] G. Hou, I.J.L. Byeon, J. Ahn, A.M. Gronenborn, T. Polenova, ^{1}H-^{13}C/^{1}H-^{15}N heteronuclear dipolar recoupling by R-symmetry sequences under fast magic angle spinning for dynamics analysis of biological and organic solids, J. Am. Chem. Soc. 133 (2011) 18646–18655. https://doi.org/10.1021/ja203771a.
[24] G. Hou, X. Lu, A.J. Vega, T. Polenova, Accurate measurement of heteronuclear dipolar couplings by phase-alternating R-symmetry (PARS) sequences in magic angle spinning NMR spectroscopy, J. Chem. Phys. 141 (2014) 104202. https://doi.org/10.1063/1.4894226.
[25] H.R.W. Dannatt, G.F. Taylor, K. Varga, V.A. Higman, M.P. Pfeil, L. Asilmovska, P.J. Judge, A. Watts, ^{13}C- and ^{1}H-detection under fast MAS for the study of poorly available proteins: application to sub-milligram quantities of a 7 trans-membrane protein, J. Biomol. NMR. 62 (2015) 17–23. https://doi.org/10.1007/s10858-015-9911-1.
[26] Y. Ji, L. Liang, X. Bao, G. Hou, Recent progress in dipolar recoupling techniques under fast MAS in solid-state NMR spectroscopy, Solid State Nucl. Magn. Reson. 112 (2021) 101711. https://doi.org/10.1016/j.ssnmr.2020.101711.
[27] Y. Ishii, I. Wickramasinghe, I. Matsuda, Y. Endo, Y. Nishiyama, T. Nemoto, T. Kamihara, Progress in proton-detected solid-state NMR (SSNMR): super-fast 2D SSNMR collection for nano-mole-scale proteins, J. Magn. Reson. 286 (2018) 99–109. https://doi.org/10.1016/j.jmr.2017.11.011.
[28] S. Asami, B. Reif, Proton-detected solid-state NMR spectroscopy at aliphatic sites: Application to crystalline systems, Acc. Chem. Res. 46 (2013) 2089–2097. https://doi.org/10.1021/ar400063y.
[29] S. Parthasarathy, Y. Nishiyama, Y. Ishii, Sensitivity and resolution enhanced solid-state NMR for paramagnetic systems and biomolecules under very fast magic angle spinning, Acc. Chem. Res. 46 (2013) 2127–2135. https://doi.org/10.1021/ar4000482.
[30] D.H. Zhou, G. Shah, M. Cormos, C. Mullen, D. Sandoz, C.M. Rienstra, Proton-detected solid-state NMR spectroscopy of fully protonated proteins at 40 kHz magic-angle spinning, J. Am. Chem. Soc. 129 (2007) 11791–11801. https://doi.org/10.1021/ja073462m.
[31] G. Kervern, G. Pintacuda, Y. Zhang, E. Oldfield, C. Roukoss, E. Kuntz, E. Herdtweck, J.M. Basset, S. Cadars, A. Lesage, C. Copéret, L. Emsley, Solid-state NMR of a paramagnetic DIAD-Fe^{II} catalyst: Sensitivity, resolution enhancement, and structure-based assignments, J. Am. Chem. Soc. 128 (2006) 13545–13552. https://doi.org/10.1021/ja063510n.
[32] V. Agarwal, S. Penzel, K. Szekely, R. Cadalbert, E. Testori, A. Oss, J. Past, A. Samoson, M. Ernst, A. Böckmann, B.H. Meier, De Novo 3D structure determination from sub-milligram protein samples by solid-state 100 kHz

MAS NMR spectroscopy, Angew. Chem. Int. Ed. 53 (2014) 12253–12256. https://doi.org/10.1002/anie.201405730.
[33] D. Cala-De Paepe, J. Stanek, K. Jaudzems, K. Tars, L.B. Andreas, G. Pintacuda, Is protein deuteration beneficial for proton detected solid-state NMR at and above 100 kHz magic-angle spinning?, Solid State Nucl. Magn. Reson. 87 (2017) 126–136. https://doi.org/10.1016/j.ssnmr.2017.07.004.
[34] M. Schledorn, A.A. Malär, A. Torosyan, S. Penzel, D. Klose, A. Oss, M.L. Org, S. Wang, L. Lecoq, R. Cadalbert, A. Samoson, A. Böckmann, B.H. Meier, Protein NMR spectroscopy at 150 kHz magic-angle spinning continues to improve resolution and mass sensitivity, ChemBioChem. 21 (2020) 2540–2548. https://doi.org/10.1002/cbic.202000341.
[35] Y. Nishiyama, Fast magic-angle sample spinning solid-state NMR at 60–100 kHz for natural abundance samples, Solid State Nucl. Magn. Reson. 78 (2016) 24–36. https://doi.org/10.1016/j.ssnmr.2016.06.002.
[36] M.K. Pandey, J.T. Damron, A. Ramamoorthy, Y. Nishiyama, Proton-detected 3D ^{1}H anisotropic/^{14}N/^{1}H isotropic chemical shifts correlation NMR under fast magic angle spinning on solid samples without isotopic enrichment, Solid State Nucl. Magn. Reson. 97 (2019) 40–45. https://doi.org/10.1016/j.ssnmr.2018.12.002.
[37] L. Duma, D. Abergel, P. Tekely, G. Bodenhausen, Proton chemical shift anisotropy measurements of hydrogen-bonded functional groups by fast magic-angle spinning solid-state NMR spectroscopy, Chem. Comm. (2008) 2361–2363. https://doi.org/10.1039/b801154k.
[38] G.A. Jeffery, Y. Yeon, The correlation between hydrogen-bond lengths and proton chemical shifts in crystals, Acta Crystallogr. B42 (1986) 410–413. https://doi.org/10.1107/S0108768186098038.
[39] B. Berglund, R.W. Vaughan, Correlations between proton chemical shift tensors, deuterium quadrupole couplings, and bond distances for hydrogen bonds in solids, J. Chem. Phys. 73 (1980) 2037–2043. https://doi.org/10.1063/1.440423.
[40] G. Wu, C.J. Freure, E. Verdurand, Proton chemical shift tensors and hydrogen bond geometry: a ^{1}H-^{2}H dipolar NMR study of the water molecule in crystalline hydrates, J. Am. Chem. Soc. 120 (1998) 13187–13193. https://doi.org/10.1021/ja983126t.
[41] R. Zhang, K.H. Mroue, A. Ramamoorthy, Proton-based ultrafast magic angle spinning solid-state NMR spectroscopy, Acc. Chem. Res. 50 (2017) 1105–1113. https://doi.org/10.1021/acs.accounts.7b00082.
[42] T. Kobayashi, F.A. Perras, Y. Nishiyama, Determination of the chemical shift tensor anisotropy and asymmetry of strongly dipolar coupled protons under fast MAS, Solid State Nucl. Magn. Reson. 114 (2021) 101743. https://doi.org/10.1016/j.ssnmr.2021.101743.
[43] M.K. Pandey, M. Malon, A. Ramamoorthy, Y. Nishiyama, Composite-180° pulse-based symmetry sequences to recouple proton chemical shift anisotropy tensors under ultrafast MAS solid-state NMR spectroscopy, J. Magn. Reson. 250 (2015) 45–54. https://doi.org/10.1016/j.jmr.2014.11.002.

[44] M.K. Pandey, J.R. Yarava, R. Zhang, A. Ramamoorthy, Y. Nishiyama, Proton-detected 3D $^{15}N/^{1}H/^{1}H$ isotropic/anisotropic/isotropic chemical shift correlation solid-state NMR at 70 kHz MAS, Solid State Nucl. Magn. Reson. 76–77 (2016) 1–6. https://doi.org/10.1016/j.ssnmr.2016.03.001.

[45] M.K. Pandey, Y. Nishiyama, Determination of NH proton chemical shift anisotropy with ^{14}N-^{1}H heteronuclear decoupling using ultrafast magic angle spinning solid-state NMR, J. Magn. Reson. 261 (2015) 133–140. https://doi.org/10.1016/j.jmr.2015.10.015.

[46] H.K. Miah, D.A. Bennett, D. Iuga, J.J. Titman, Measuring proton shift tensors with ultrafast MAS NMR, J. Magn. Reson. 235 (2013) 1–5. https://doi.org/10.1016/j.jmr.2013.07.005.

[47] J.C.C. Chan, R. Tycko, Recoupling of chemical shift anisotropies in solid-state NMR under high-speed magic-angle spinning and in uniformly ^{13}C-labeled systems, J. Chem. Phys. 118 (2003) 8378–8389. https://doi.org/10.1063/1.1565109.

[48] E. Nehra, N. Sehrawat, T. Kobayashi, Y. Nishiyama, M.K. Pandey, Proton-detected ^{15}N-^{1}H dipolar coupling/^{1}H chemical shift correlation experiment for the measurement of NH distances in biological solids under fast MAS solid-state NMR, J. Magn. Reson. Open. 10–11 (2022) 100028. https://doi.org/10.1016/j.jmro.2021.100028.

[49] B. Heise, J. Leppert, R. Ramachandran, Characterization of ^{15}N chemical shift tensors via ^{15}N-^{13}C REDOR and ^{15}N-^{1}H dipolar-shift CPMAS NMR spectroscopy, Solid State Nucl. Magn. Reson. 16 (2000) 177–187. https://doi.org/10.1016/s0926-2040(00)00073-4.

[50] M.K. Pandey, Y. Nishiyama, Determination of relative orientation between ^{1}H CSA tensors from a 3D solid-state NMR experiment mediated through $^{1}H/^{1}H$ RFDR mixing under ultrafast MAS, Solid State Nucl. Magn. Reson. 70 (2015) 15–20. https://doi.org/10.1016/j.ssnmr.2015.05.001.

[51] G. Hou, S. Paramasivam, I.J.L. Byeon, A.M. Gronenborn, T. Polenova, Determination of relative tensor orientations by γ-encoded chemical shift anisotropy/heteronuclear dipolar coupling 3D NMR spectroscopy in biological solids, Phys. Chem. Chem. Phys. 12 (2010) 14873–14883. https://doi.org/10.1039/c0cp00795a.

[52] G. Hou, S. Paramasivam, S. Yan, T. Polenova, A.J. Vega, Multidimensional magic angle spinning NMR spectroscopy for site-resolved measurement of proton chemical shift anisotropy in biological solids, J. Am. Chem. Soc. 135 (2013) 1358–1368. https://doi.org/10.1021/ja3084972.

[53] C.H. Wu, A. Ramamoorthy, L.M. Gierasch, S.J. Opella, Simultaneous characterization of the amide ^{1}H Chemical Shift, ^{1}H-^{15}N dipolar, and ^{15}N chemical shift interaction tensors in a peptide bond by three-dimensional solid-state NMR spectroscopy, J. Am. Chem. Soc. 117 (1995) 6148–6149. https://doi.org/10.1021/ja00127a039.

[54] A. Ramamoorthy, C.H. Wu, S.J. Opella, Magnitudes and orientations of the principal elements of the ^{1}H chemical shift, ^{1}H-^{15}N dipolar coupling, and ^{15}N chemical shift interaction tensors in $^{15}N_{\varepsilon 1}$-Tryptophan and $^{15}N_{\pi}$-histidine side chains determined by three-dimensional solid-state NMR spectroscopy

of polycrystalline samples, J. Am. Chem. Soc. 119 (1997) 10479–10486. https://doi.org/10.1021/ja9632670.
[55] D.K. Lee, Y. Wei, A. Ramamoorthy, A two-dimensional magic-angle decoupling and magic-angle turning solid-state NMR method: an application to study chemical shift tensors from peptides that are nonselectively labeled with ^{15}N isotope, J. Phys. Chem. B. 105 (2001) 4752–4762. https://doi.org/10.1021/jp002902s.
[56] D.K. Lee, R.J. Wittebort, A. Ramamoorthy, Characterization of ^{15}N chemical shift and ^{1}H-^{15}N dipolar coupling interactions in a peptide bond of uniaxially oriented and polycrystalline samples by one-dimensional dipolar chemical shift solid-state NMR spectroscopy, J. Am. Chem. Soc. 120 (1998) 8868–8874. https://doi.org/10.1021/ja981599u.
[57] L. Liang, Y. Ji, K. Chen, P. Gao, Z. Zhao, G. Hou, Solid-state NMR dipolar and chemical shift anisotropy recoupling techniques for structural and dynamical studies in biological systems, Chem. Rev. 122 (2022) 9880–9942. https://doi.org/10.1021/acs.chemrev.1c00779.
[58] G. Hou, R. Gupta, T. Polenova, A.J. Vega, A magic-angle-spinning NMR spectroscopy method for the site-specific measurement of proton chemical-shift anisotropy in biological and organic solids, Isr. J. Chem. 54 (2014) 171–183. https://doi.org/10.1002/ijch.201300099.
[59] G. Metz, X.L. Wu, S.O. Smith, Ramped-amplitude cross polarisation in magic-angle spinning NMR, J. Magn. Reson. A. 110 (1994) 219–227. https://doi.org/10.1006/jmra.1994.1208.
[60] M.H. Levitt, Symmetry-based pulse sequences in magic-angle spinning solid-state NMR, EMagRes. 9 (2002) 165–196. http://dx.doi.org/10.1002/9780470034590.emrstm0551.
[61] M.M. Maricq, J.S. Waugh, NMR in rotating solids, J. Chem. Phys. 70 (1979) 3300–3316. https://doi.org/10.1063/1.437915.
[62] B.H. Meier, Cross polarization under fast magic angle spinning: thermodynamical considerations, Chem. Phys. Lett. 188 (1992) 201–207. https://doi.org/10.1016/0009-2614(92)90009-C.
[63] Y. Nishiyama, M. Malon, Y. Ishii, A. Ramamoorthy, 3D ^{15}N/^{15}N/^{1}H chemical shift correlation experiment utilizing an RFDR-based ^{1}H/^{1}H mixing period at 100 kHz MAS, J. Magn. Reson. 244 (2014) 1–5. https://doi.org/10.1016/j.jmr.2014.04.008.
[64] M. Bak, J.T. Rasmussen, N.C. Nielsen, SIMPSON: a general simulation program for solid-state NMR spectroscopy, J. Magn. Reson. 147 (2000) 296–330. https://doi.org/10.1006/jmre.2000.2179.
[65] Z. Tošner, R. Andersen, B. Stevensson, M. Edén, N.C. Nielsen, T. Vosegaard, Computer-intensive simulation of solid-state NMR experiments using SIMPSON, J. Magn. Reson. 246 (2014) 79–93. https://doi.org/10.1016/j.jmr.2014.07.002.
[66] M. Bak, N.C. Nielsen, Repulsion, a novel approach to efficient powder averaging in solid-state NMR, J. Magn. Reson. 125 (1997) 132–139. https://doi.org/10.1006/ jmre.1996.1087.

[67] H. Fuess, D. Hohlwein, S.A. Mason, Neutron diffraction study of L-histidine hydrochloride monohydrate, Acta Crystallogr. B33 (1977) 654–659. https://doi. org/10.1107/S0567740877004415.
[68] P. Paluch, T. Pawlak, J.P. Amoureux, M.J. Potrzebowski, Simple and accurate determination of X-H distances under ultra-fast MAS NMR, J. Magn. Reson. 233 (2013) 56–63. https://doi.org/10.1016/j.jmr.2013.05.005.
[69] Y. Nishiyama, M. Malon, M.J. Potrzebowski, P. Paluch, J.P. Amoureux, Accurate NMR determination of C-H or N-H distances for unlabeled molecules, Solid State Nucl. Magn. Reson. 73 (2016) 15–21. https://doi.org/10.1016/j.ssnmr.2015.06.005.
[70] F. James, M. Roos, Minuit - a system for function minimization and analysis of the parameter errors and correlations, Comput. Phys. Commun. 10 (1975) 343–367. https://doi.org/10.1016/0010-4655(75)90039-9.

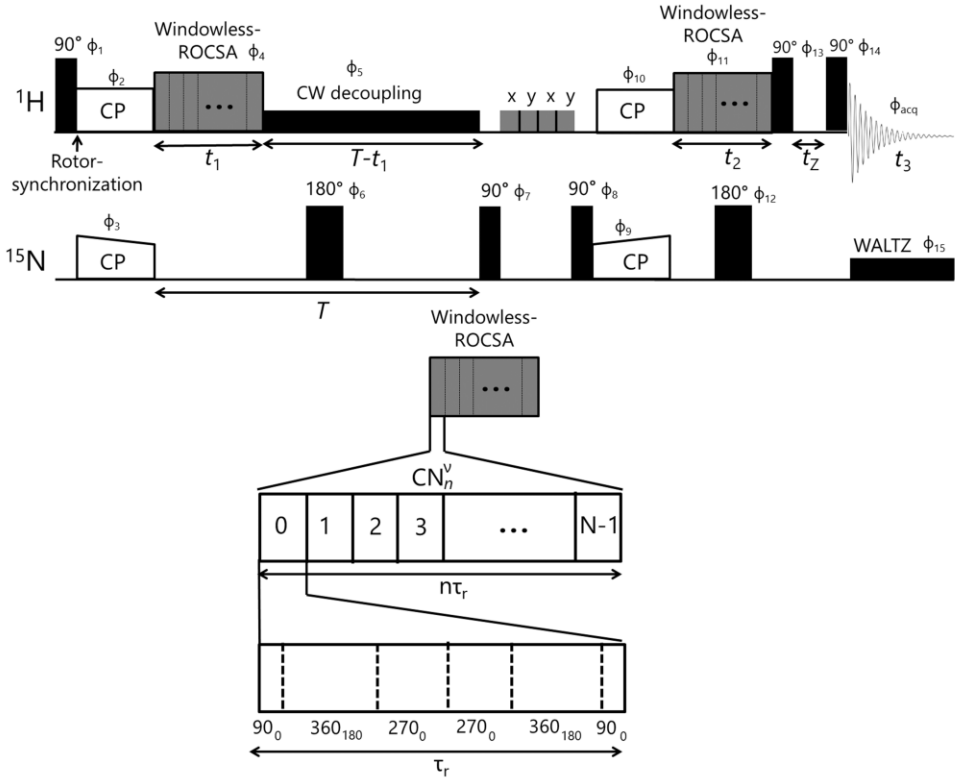

Figure 1: Pulse sequence for the proton-detected 3D ^{15}N-^{1}H DIP/^{1}H CSA/^{1}H CS correlation experiment to get the relative orientation between ^{15}N-^{1}H DIP and ^{1}H CSA tensors. The phase cycling scheme implemented in the pulse sequence is as follows: ϕ_1 = {0°}, ϕ_2 = {90°}, ϕ_3 = {0°}, ϕ_4 = {0°}, ϕ_5 = {0°}, ϕ_6 = {2(0°), 2(90°), 2(180°), 2(270°)}, ϕ_7 = {90°}, ϕ_8 = {270°}, ϕ_9 = {0°}, ϕ_{10} = {0°, 180°}, ϕ_{11} = {0°}, ϕ_{12} = {0°}, ϕ_{13} =

{8(90°), 8(270°)}, ϕ_{14} = {16(0°), 16(120°), 16(240°)}, ϕ_{acq} = {2(0°, 180°, 180°, 0°), 2(180°, 0°, 0°, 180°), 2(120°, 300°, 300°, 120°), 2(300°, 120°, 120°, 300°), 2(240°, 60°, 60°, 240°), 2(60°, 240°, 240°, 60°)}, ϕ_{15} = {0°}.

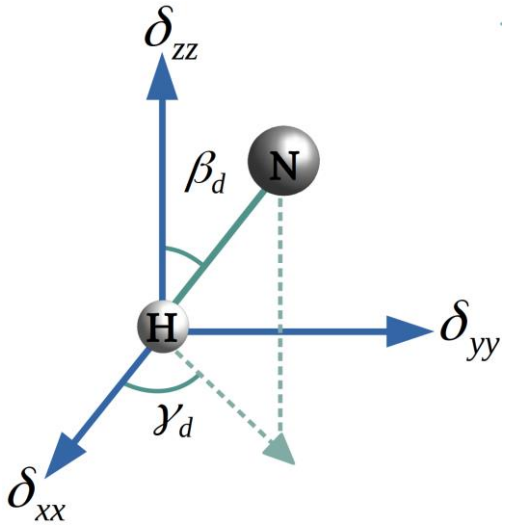

Figure 2: Depiction of the relative orientation of the ^{1}H CSA and ^{15}N-^{1}H DIP tensors in the molecular axis system (MolAS). In this representation, the PAS of the ^{1}H CSA tensor is considered coincident with the MolAS. The two angles, β_d and γ_d represent the polar and azimuthal angles of the NH dipolar vector in the PAS of the ^{1}H CSA tensor, respectively, and therefore, the relative orientation between ^{1}H CSA and ^{15}N-^{1}H DIP tensors.

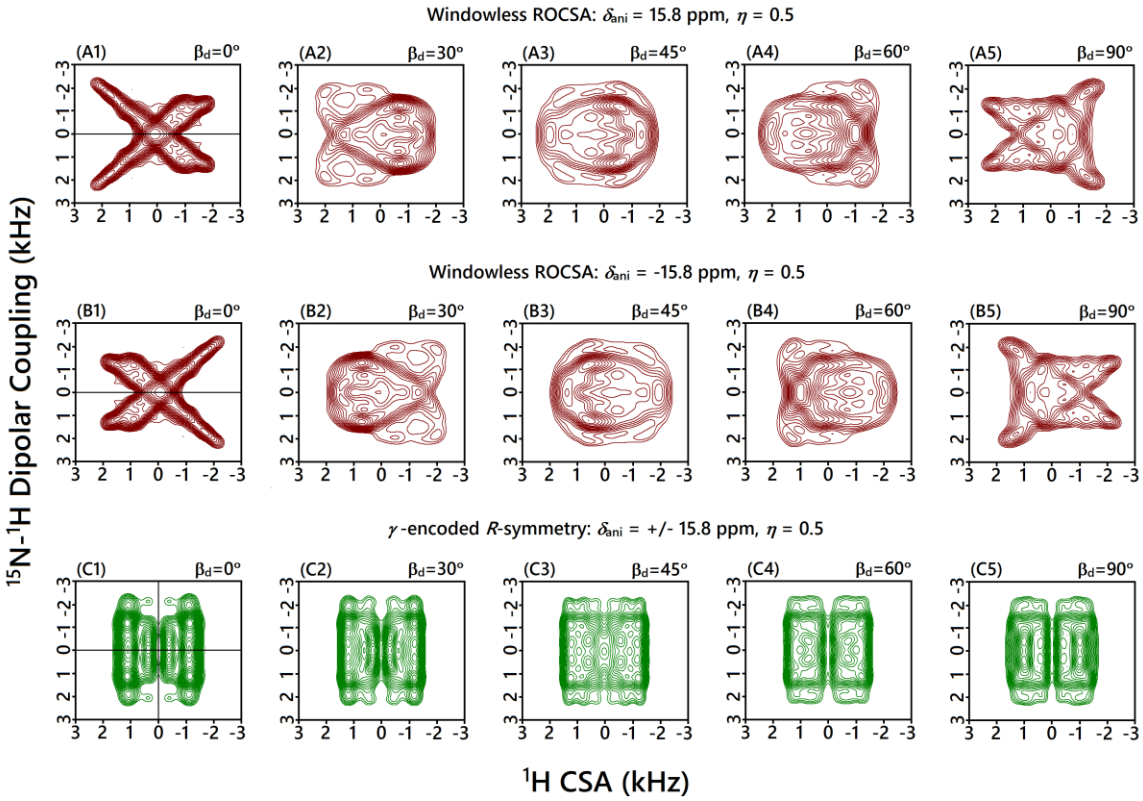

Figure 3: Simulated 2D ^{15}N-^{1}H DIP/^{1}H CSA powder lineshapes obtained with a variation in the β_d angles for constant ^{1}H CSA parameters (δ_{ani} = ± 15.8 ppm; η = 0.5) and the ^{15}N-^{1}H DIP constant (9.6 kHz) from the SIMPSON software using the proposed windowless $C3_3^1$-ROCSA-based [top (δ_{ani} = 15.8 ppm) and middle (δ_{ani} = -15.8 ppm)] panels, and the γ-encoded $R18_8^7(270^\circ 90^\circ)$-symmetry-based (bottom panel) correlation methods. All the simulations were carried out using REPULSION-168 (α, β) crystallite orientations and 60 γ-angles with a maximum time step (0.1 μs) under a MAS rate of 62.5 kHz. Zero filling with twelve times the data size and a single exponential function (line broadening of 200 Hz) were applied before the Fourier transform of the simulated time-domain signals in the DIP and CSA dimensions.

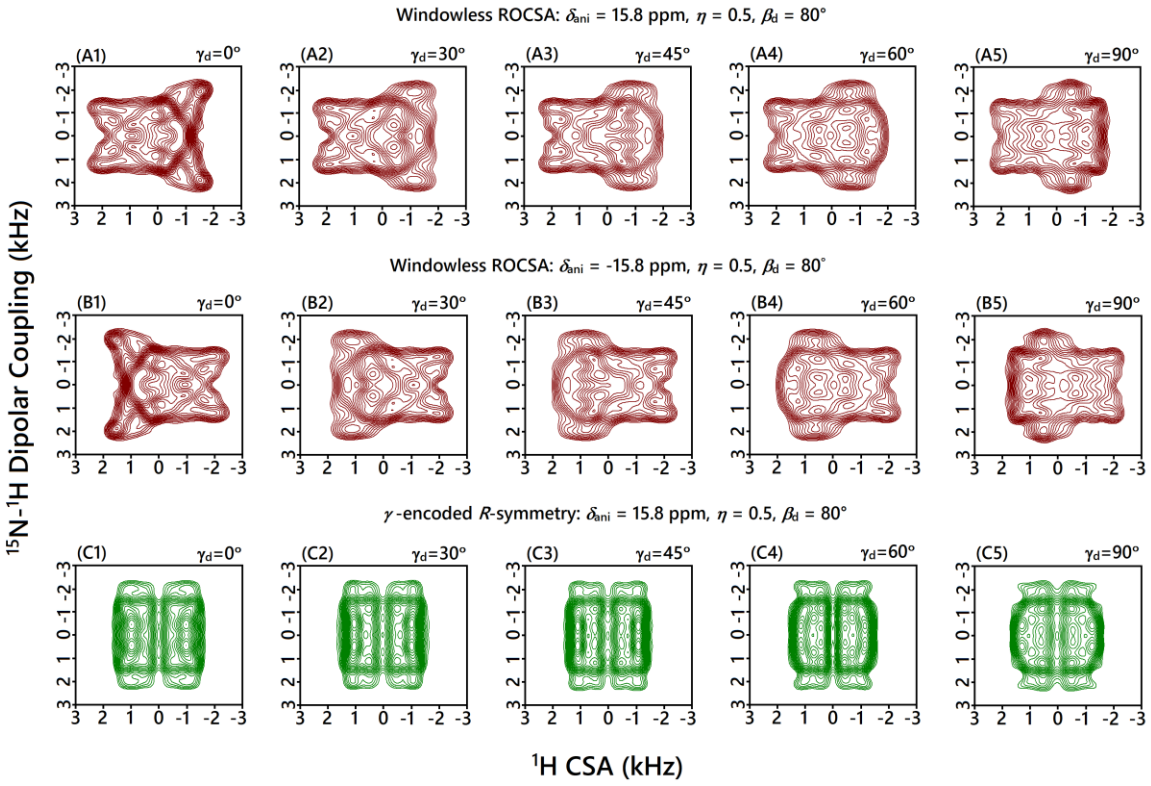

Figure 4: Simulated 2D ^{15}N-^{1}H DIP/^{1}H CSA powder lineshapes obtained with a variation in the γ_d angles for a constant ^{1}H CSA parameters (δ_{ani} = ± 15.8 ppm; η = 0.5) and the ^{15}N-^{1}H DIP constant (9.6 kHz) from the SIMPSON software using the proposed windowless $C3_3^1$-ROCSA-based [top (δ_{ani} = 15.8 ppm) and middle (δ_{ani} = -15.8 ppm)] panels, and γ-encoded $R18_8^7(270^\circ 90^\circ)$ -symmetry-based (bottom panel) correlation methods. The remaining simulation parameters are as given in the caption of **Figure 3**.

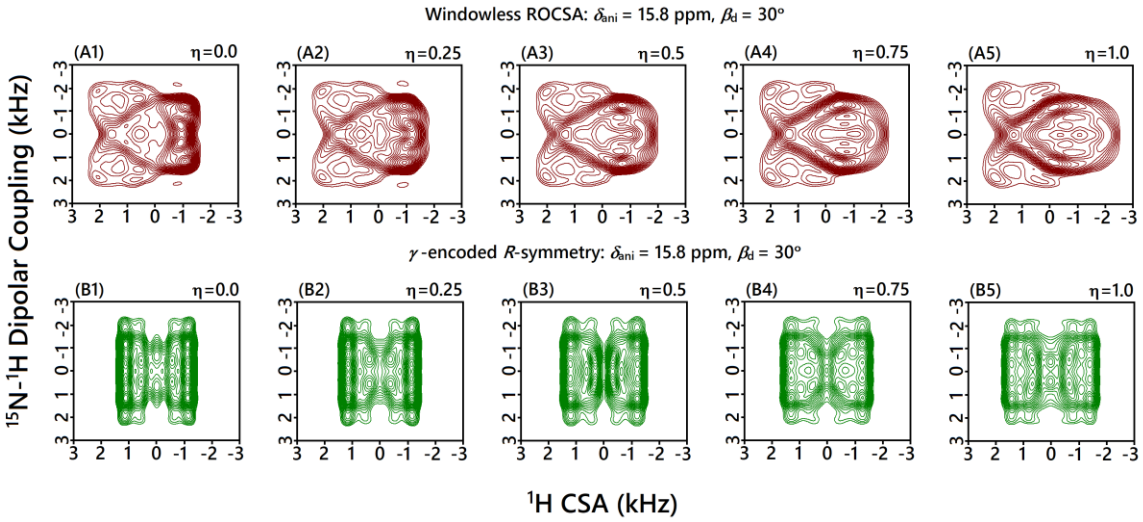

Figure 5: Simulated 2D ^{15}N-^{1}H DIP/^{1}H CSA powder lineshapes obtained with a variation in the ^{1}H CSA asymmetry parameter (η) at fixed β_d = 30°, the ^{1}H CSA (δ_{ani} = 15.8 ppm) and the ^{15}N-^{1}H DIP constant (9.6 kHz) from the SIMPSON software using the proposed windowless $C3_3^1$ -ROCSA-based (top panel), and the γ-encoded $R18_8^7(270^\circ 90^\circ)$ -symmetry-based (bottom panel) correlation methods. The remaining simulation parameters are as given in the caption of **Figure 3**.

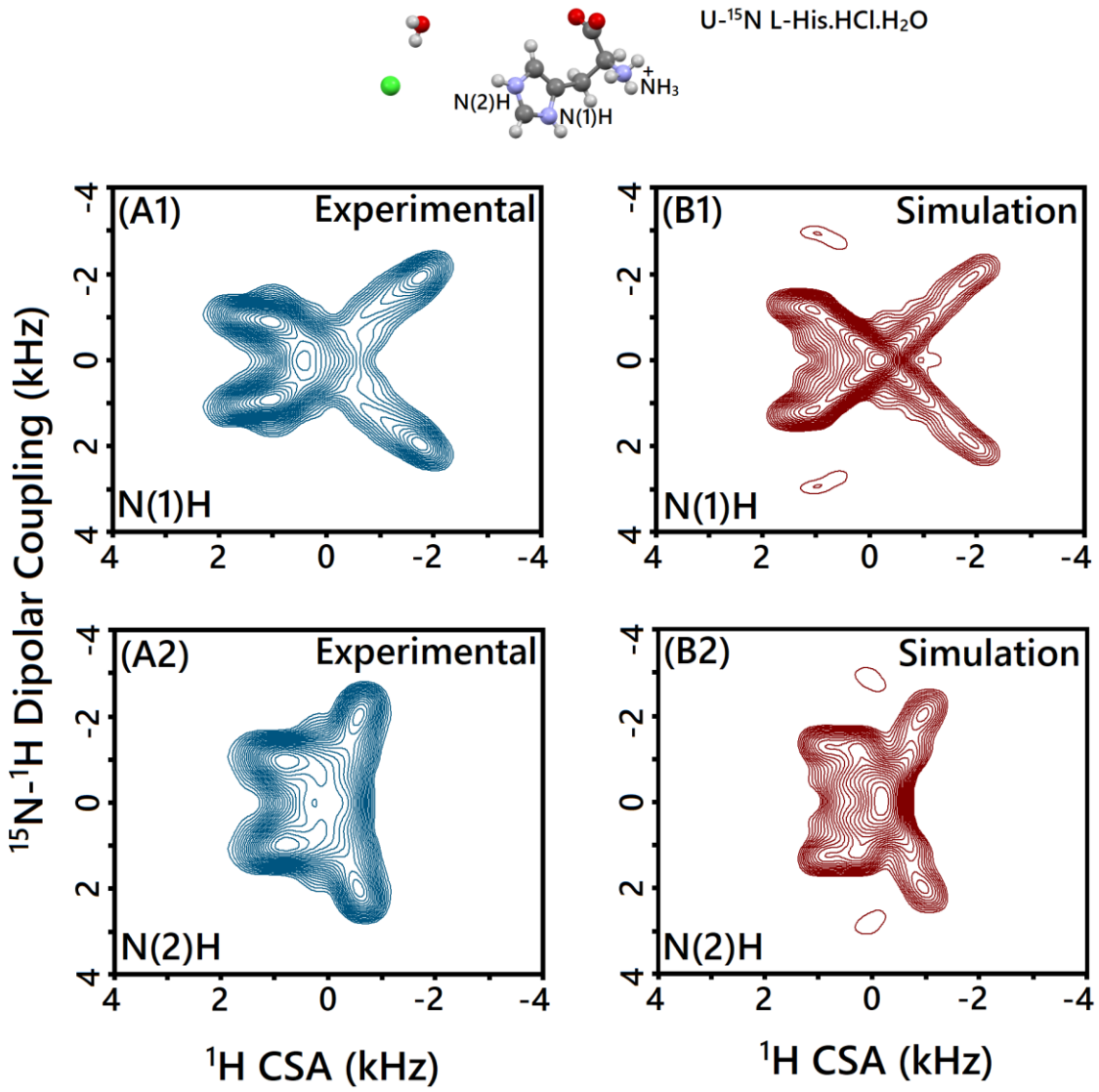

Figure 6: Experimental (blue) 2D ^{15}N-^{1}H DIP/^{1}H CSA correlation spectra of U-^{15}N L-His.HCl.H_2O [(A1): N(1)H and (A2): N(2)H)] extracted by taking a slice at respective NH proton isotropic chemical shifts (CS) of the 3D ^{15}N-^{1}H DIP/^{1}H CSA/^{1}H CS spectrum. Simulated 2D ^{15}N-^{1}H DIP/^{1}H CSA spectra (maroon) obtained from the SIMPSON software are represented in the right panel [(B1): N(1)H and (B2): N(2)H)]. All the simulations were carried out using REPULSION-168 (α, β) crystallite orientations and 60 γ-angles with a maximum time step (0.1 μs) under a MAS rate of 69.832 kHz. Zero filling with twelve times the data size along with a single exponential function (line broadening of 200 Hz) was applied before the Fourier transform of the simulated time-domain signals in the dipolar coupling and CSA dimensions.

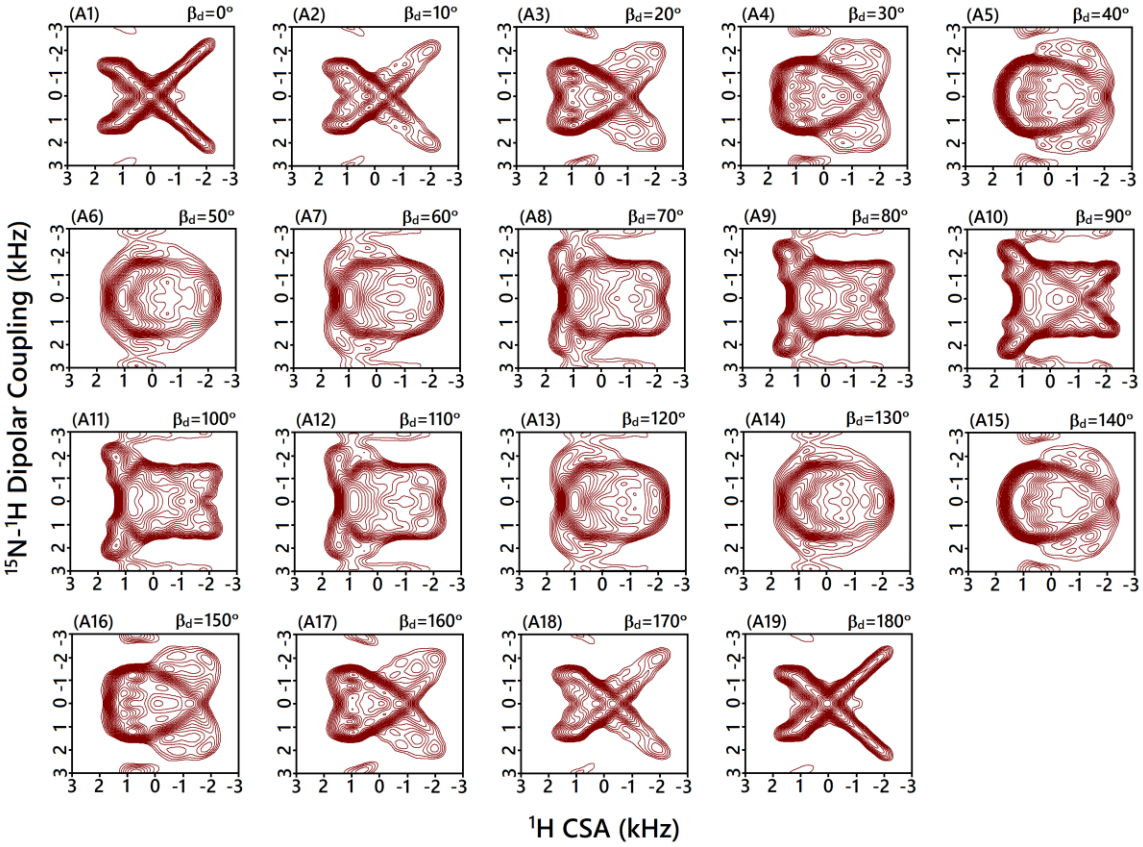

Figure 7: Simulated 2D ^{15}N-^{1}H DIP/^{1}H CSA powder spectra obtained from the SIMPSON software with a variation of dipolar PAS angle β_d, and fixed α_d and γ_d = 0°. All the simulations were carried out with the ^{15}N-^{1}H DIP constant (9.5 kHz) and ^{1}H CSA parameters (δ_{ani} = -15.3 ppm, η = 0.35) corresponding to the N(1)H group of U-^{15}N L-His.HCl.H_2O. The remaining simulation parameters are as given in the caption of **Figure 6**.

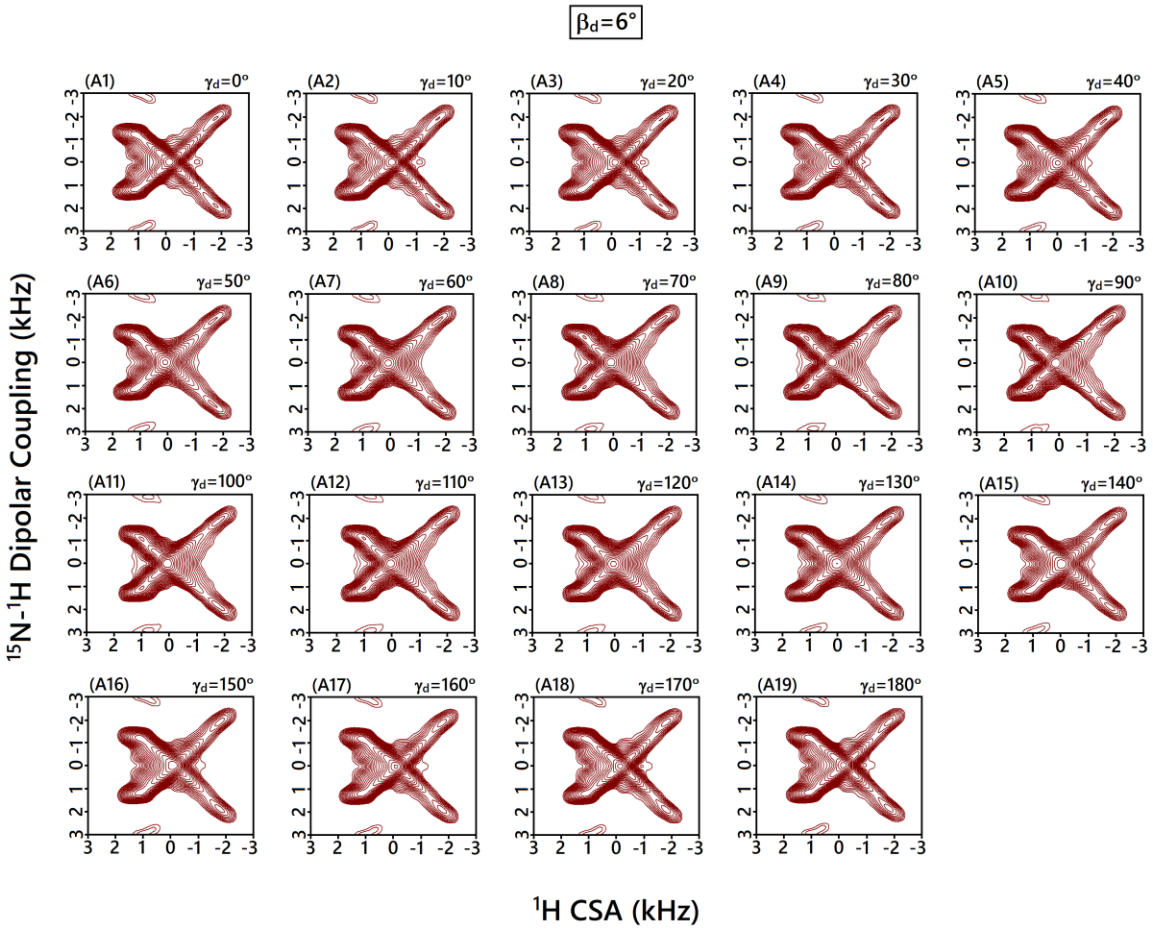

Figure 8: Simulated 2D ^{15}N-^{1}H DIP/^{1}H CSA powder spectra obtained from the SIMPSON software with a variation of dipolar PAS angle γ_d, and fixed α_d = 0° and β_d = 6°. The remaining simulation parameters are as given in the caption of **Figure 7**.

Supporting Information

Determination of the relative orientation between ^{15}N-^{1}H dipolar coupling and ^{1}H chemical shift anisotropy tensors under fast MAS solid-state NMR

Neelam Sehrawat[a,1], Ekta Nehra[a,1], Ketan Kumar Rohilla[a], Takeshi Kobayashi[b], Yusuke Nishiyama[c,d,*], Manoj Kumar Pandey[a,*]

[a] Indian Institute of Technology (IIT) Ropar, Rupnagar, Punjab, 140001, India

[b] U.S. DOE, Ames Laboratory, Iowa State University, Ames, IA, 50011-3020, United States

[c] RIKEN-JEOL Collaboration Center, RIKEN, Yokohama, Kanagawa, 230-0045, Japan

[d] JEOL RESONANCE Ltd., Musashino, Akishima, Tokyo, 196-8558, Japan

* Authors to whom correspondence should be addressed: mkpandey@iitrpr.ac.in, yunishiy@jeol.co.jp

[1] These authors contributed equally to this work

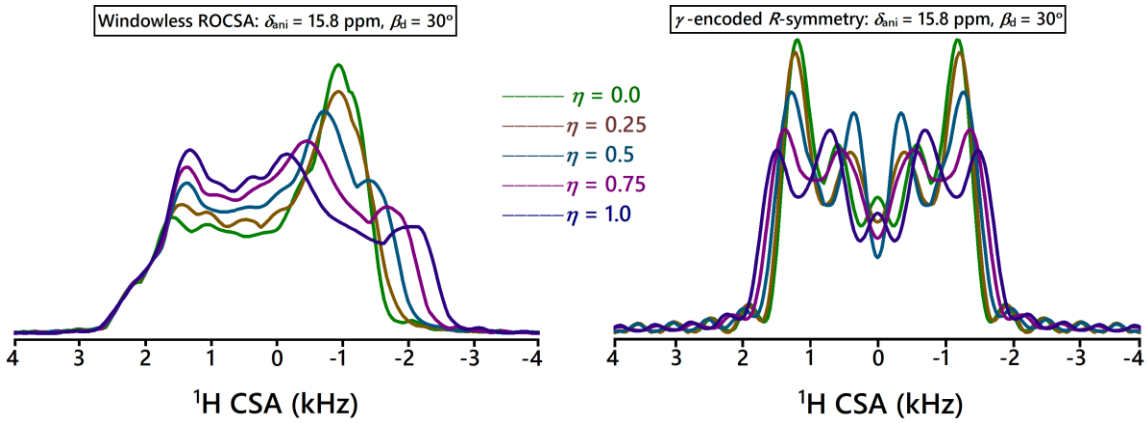

Figure S1: One-dimensional projections along the ^{1}H CSA dimension of the simulated 2D ^{15}N-^{1}H DIP/^{1}H CSA spectra shown in **Figure 5**. The colour scheme represents the variation in the ^{1}H CSA asymmetry parameter (η) for a fixed β_d = 30°, ^{1}H CSA (δ_{ani} = 15.8 ppm) and the ^{15}N-^{1}H dipolar coupling strength (9.6 kHz) using the proposed windowless $C3_3^1$ -ROCSA-based, and γ-encoded $R18_8^7(270^\circ 90^\circ)$ -symmetry-based correlation methods.

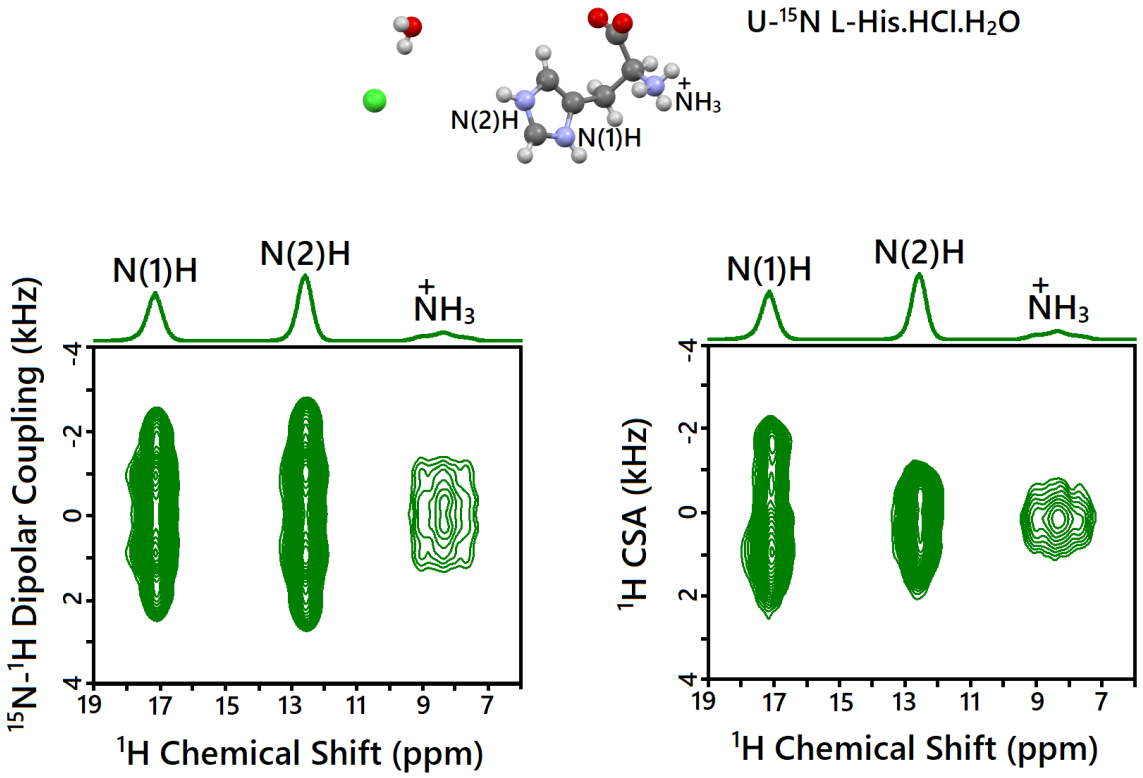

Figure S2: Chemical structure and two-dimensional (2D) ^{15}N-^{1}H DIP/^{1}H CS and ^{1}H CSA/^{1}H CS planes extracted from the 3D ^{15}N-^{1}H DIP/^{1}H CSA/^{1}H CS spectrum of U-^{15}N L-His.HCl.H_2O. The 1D traces are the projections of the 2D ^{15}N-^{1}H DIP/^{1}H CS and ^{1}H CSA/^{1}H CS correlation spectra onto the ^{1}H CS axes.

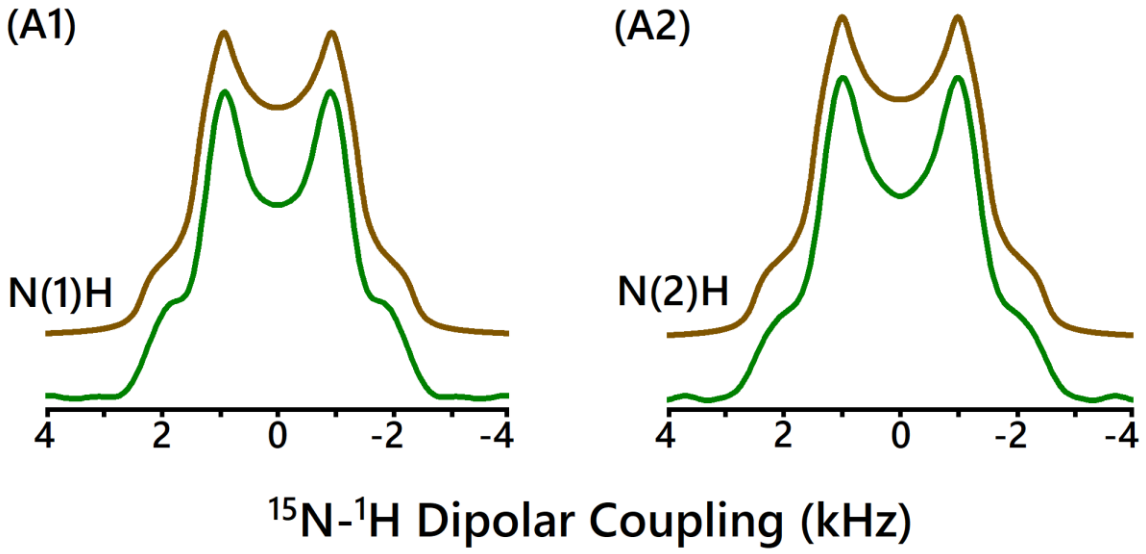

Figure S3: Experimental (green) ^{15}N-^{1}H DIP powder lineshapes extracted from the 2D ^{15}N-^{1}H DIP/^{1}H CS planes of the 3D ^{15}N-^{1}H DIP/^{1}H CSA/^{1}H CS spectrum of U-^{15}N L-His.HCl.H_2O [(A1): N(1)H and (A2): N(2)H]. The ^{15}N-^{1}H DIP powder lineshapes are obtained by taking spectral slices parallel to the recoupled ^{15}N-^{1}H DIP dimension at respective ^{1}H isotropic chemical shifts (CS). Best-fitted simulated ^{15}N-^{1}H dipolar powder lineshapes from the SIMPSON software are shown in brown. Simulations were carried out with REPULSION-678 (α, β) crystallite orientations and 60 γ-angles in a two-spin (^{15}N-^{1}H) model framework. Simulated data were processed using zero filling with eight times the data size and a single exponential function with a line broadening of 300 Hz before the application of the Fourier transform of the time domain ^{15}N-^{1}H DIP modulated signal.

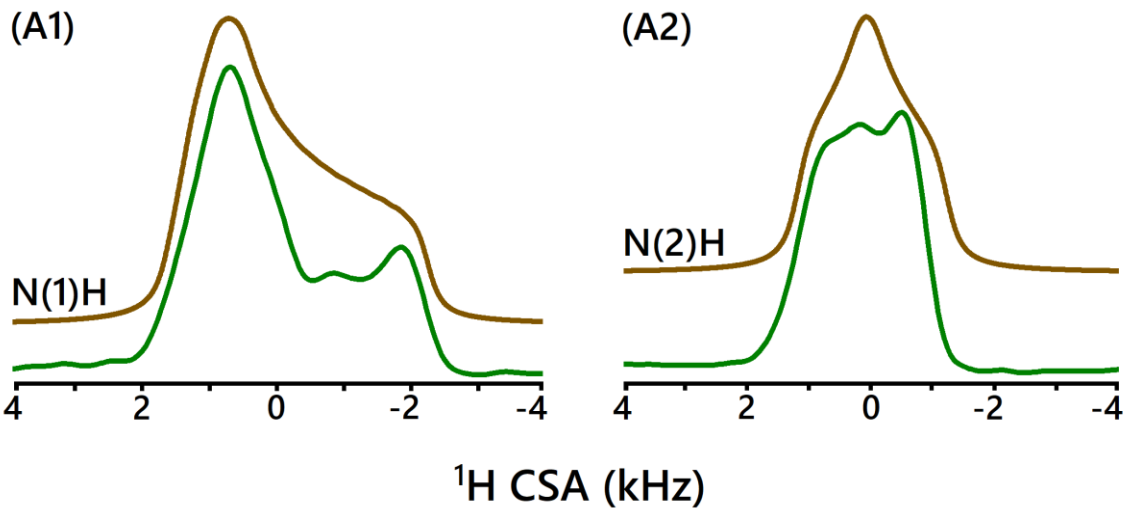

Figure S4: Experimental (green) ^{1}H CSA powder lineshapes extracted from the 2D planes ^{1}H CSA/^{1}H CS of the 3D ^{15}N-^{1}H DIP/^{1}H CSA/^{1}H CS spectrum of U-^{15}N L-His.HCl.H_2O [(A1): N(1)H and (A2): N(2)H]. The ^{1}H CSA powder lineshapes are obtained by taking spectral slices parallel to the recoupled ^{1}H CSA dimension at respective ^{1}H isotropic chemical shifts (CS). Best-fitted simulated ^{1}H CSA powder lineshapes from the SIMPSON software are shown in brown. Simulations were carried out with REPULSION-678 (α, β) crystallite orientations and 60 γ-angles in a single spin model framework. Simulated data were processed using zero filling with eight times the data size and a single exponential function with line broadening of 300 Hz before the application of the Fourier transform of the time domain ^{1}H CSA modulated signal.

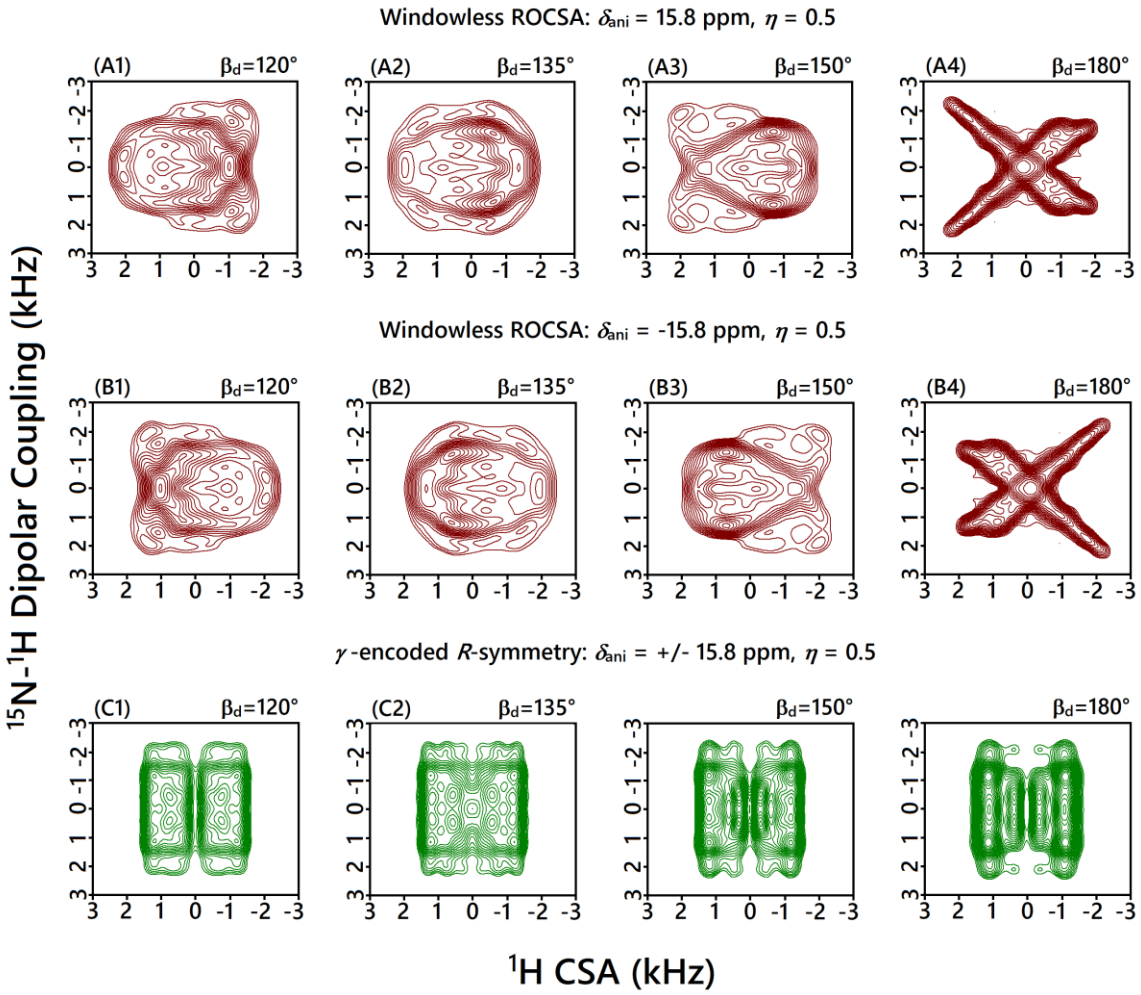

Figure S5: Simulated 2D ^{15}N-^{1}H DIP/^{1}H CSA powder lineshapes obtained with a variation in the β_d angles for a constant ^{1}H CSA parameters (δ_{ani} = ± 15.8 ppm; η = 0.5) and the ^{15}N-^{1}H DIP constant (9.6 kHz) from the SIMPSON software using the proposed windowless $C3_3^1$-ROCSA-based [top (δ_{ani} = 15.8 ppm) and middle (δ_{ani} = -15.8 ppm)] panels, and γ-encoded $R18_8^7(270^\circ 90^\circ)$ -symmetry-based (bottom panel) correlation methods. All the simulations were carried out using REPULSION-168 (α, β) crystallite orientations and 60 γ-angles with a maximum time step (0.1 μs) under a MAS rate of 62.5 kHz. Zero filling with twelve times the data size and a single exponential function (line broadening of 200 Hz) were applied before the Fourier transform of the simulated time-domain signals in the DIP and CSA dimensions.

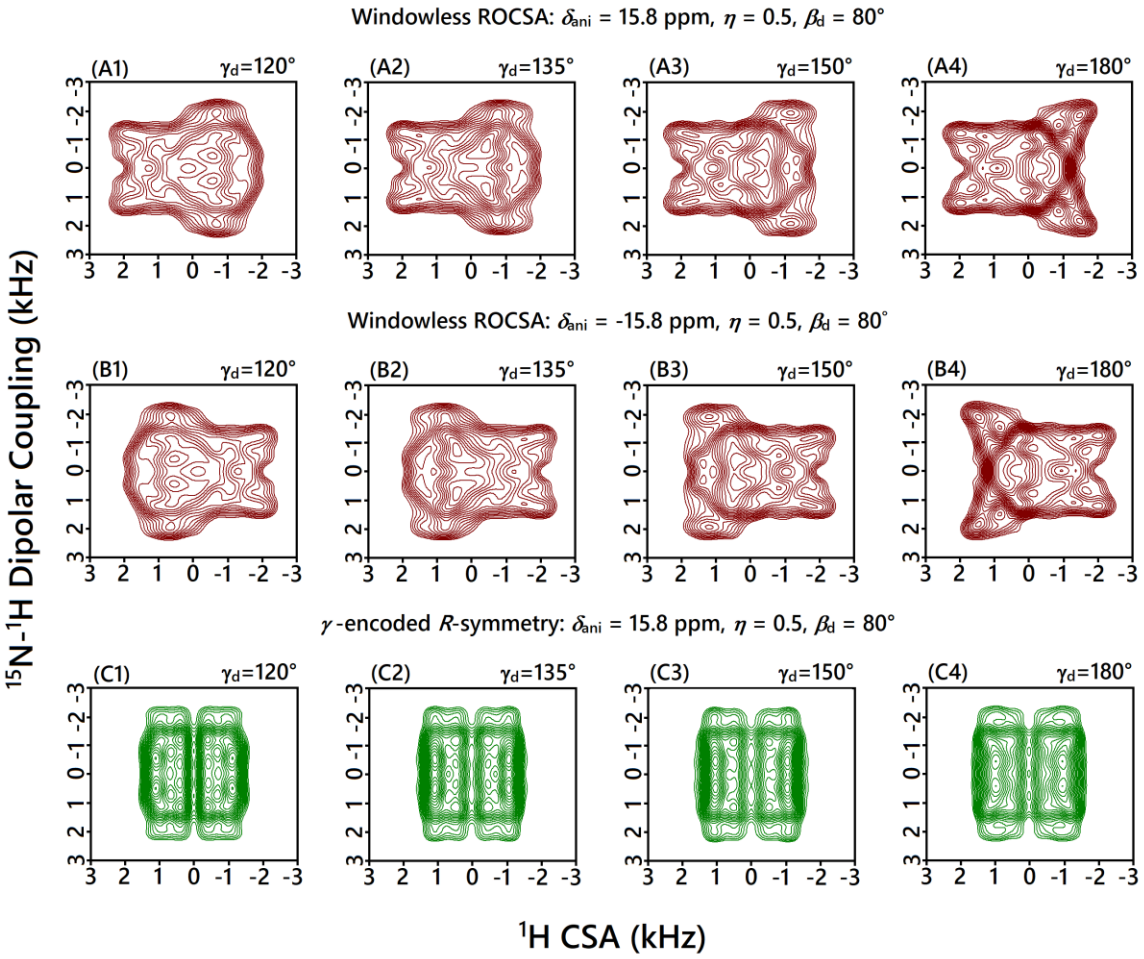

Figure S6: Simulated 2D ^{15}N-^{1}H DIP/^{1}H CSA powder lineshapes obtained with a variation in the γ_d angles for a constant ^{1}H CSA parameters (δ_{ani} = ± 15.8 ppm; η = 0.5) and the ^{15}N-^{1}H DIP constant (9.6 kHz) from the SIMPSON software using the proposed windowless $C3_3^1$-ROCSA-based [top (δ_{ani} = 15.8 ppm) and middle (δ_{ani} = -15.8 ppm)] panels, and γ-encoded $R18_8^7(270^\circ 90^\circ)$ -symmetry-based (bottom panel) correlation methods. The remaining simulation parameters are as given in the caption of **Figure 3**.

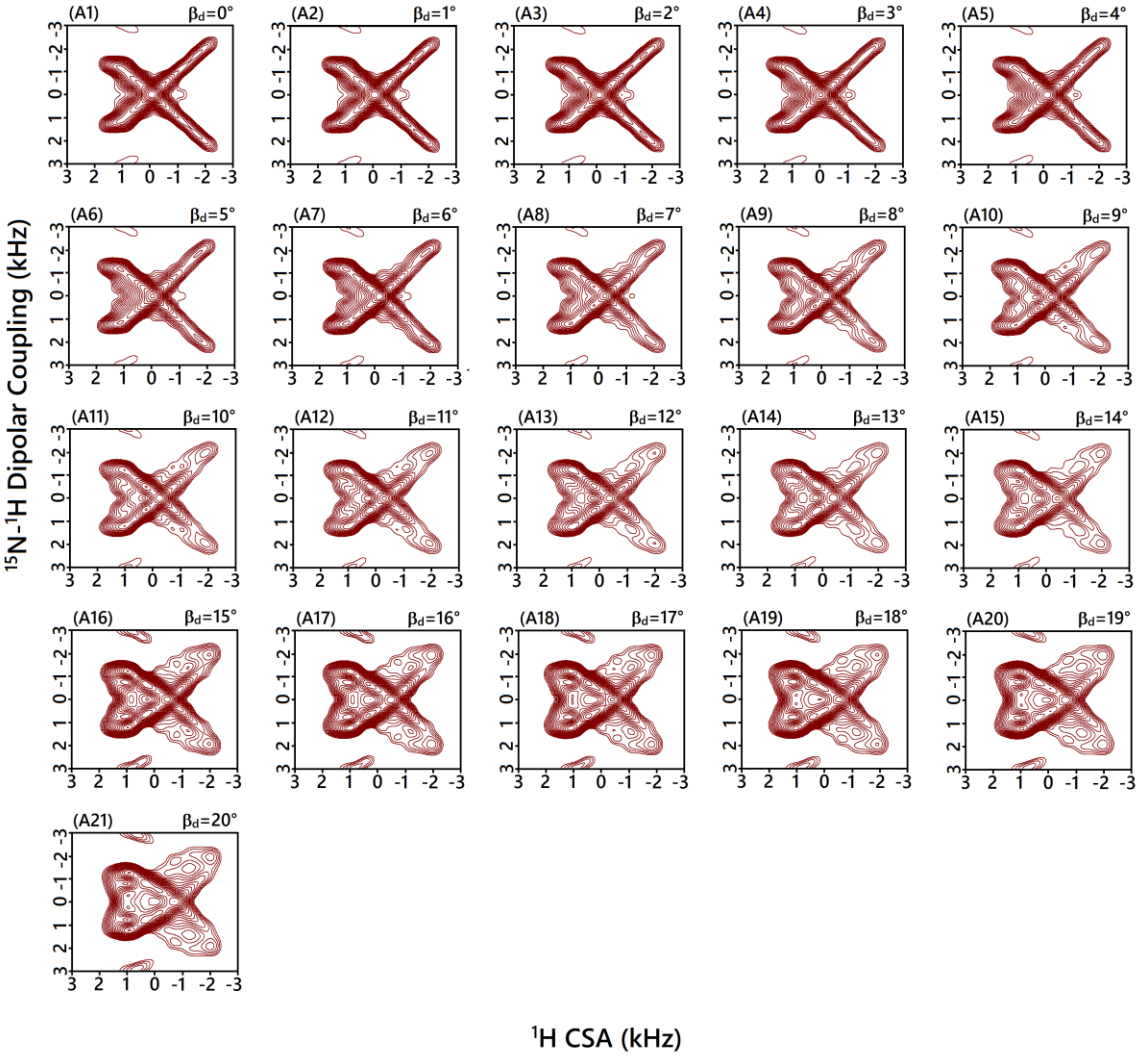

Figure S7: Simulated 2D ^{15}N-^{1}H DIP/^{1}H CSA powder spectra obtained from the SIMPSON software with a variation of dipolar PAS angle β_d (0° to 20°) with an increment of 1°, and fixed α_d and γ_d = 0°. All the simulations were carried out with the ^{15}N-^{1}H DIP constant (9.5 kHz) and ^{1}H CSA parameters (δ_{ani} = -15.3 ppm, η = 0.35) corresponding to the N(1)H group of U-^{15}N L-His.HCl.H_2O. The remaining simulation parameters are as given in the caption of **Figure 6**.

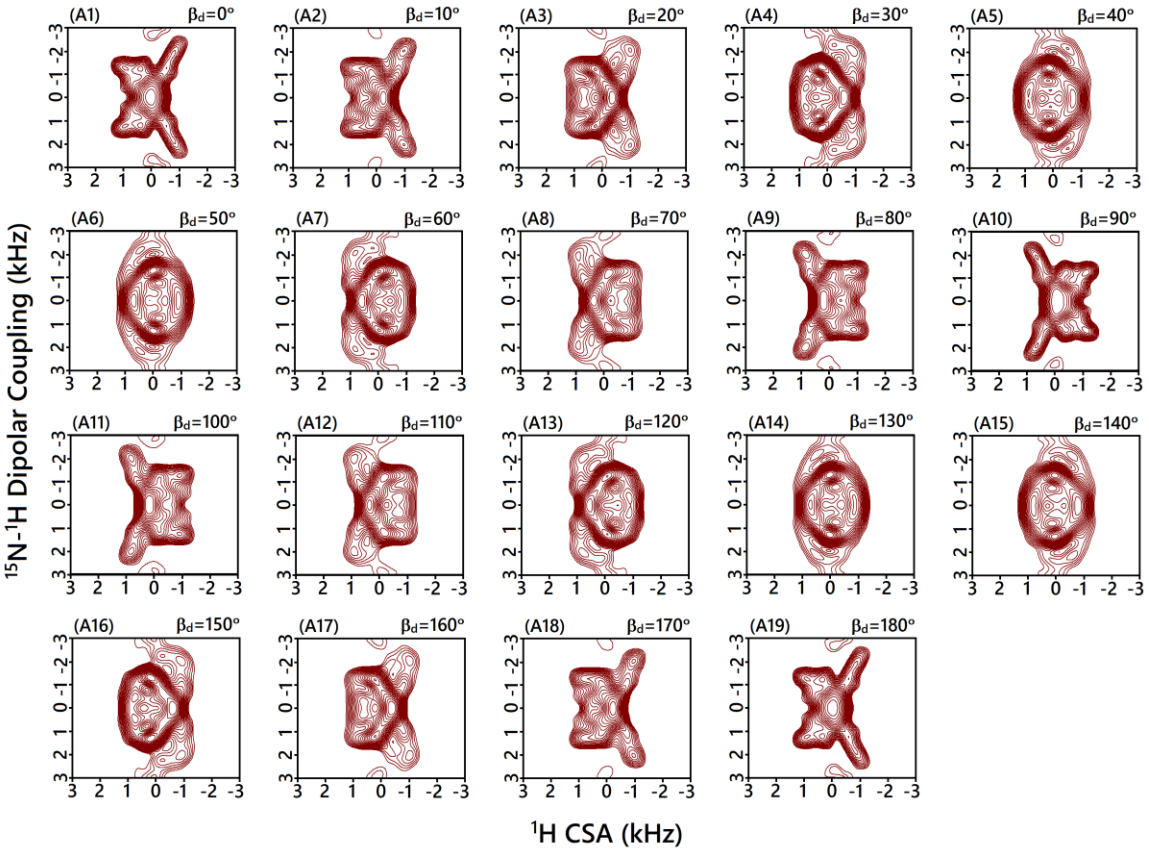

Figure S8: Simulated 2D ^{15}N-^{1}H DIP/^{1}H CSA powder spectra obtained from the SIMPSON software with a variation of dipolar PAS angle β_d, and fixed α_d and γ_d = 0°. All the simulations were carried out with the ^{15}N-^{1}H DIP constant (10.1 kHz) and ^{1}H CSA values (δ_{ani} = -7.8 ppm, η = 0.9) corresponding to the N(2)H group in the imidazole ring of U-^{15}N L-His.HCl.H_2O. The remaining simulation parameters are as given in the caption of **Figure 6**.

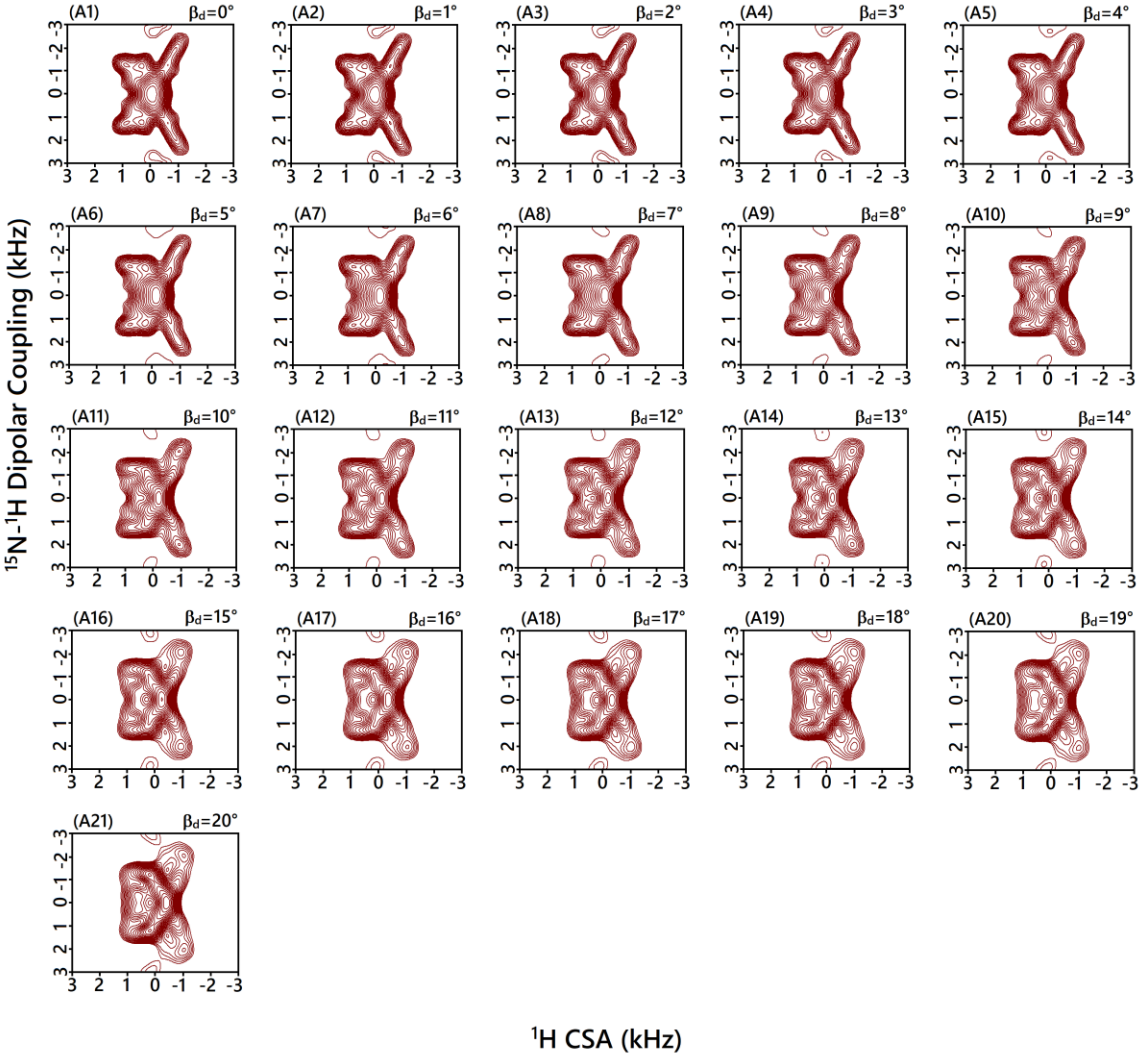

Figure S9: Simulated 2D ^{15}N-^{1}H DIP/^{1}H CSA powder spectra obtained from the SIMPSON software with a variation of dipolar PAS angle β_d (0° to 20°) with an increment of 1°, and fixed α_d and γ_d = 0°. All the simulations were carried out with the ^{15}N-^{1}H DIP constant (10.1 kHz) and ^{1}H CSA parameters (δ_{ani} = -7.8 ppm, η = 0.9) corresponding to the N(2)H group of U-^{15}N L-His.HCl.H_2O. The remaining simulation parameters are as given in the caption of **Figure 6**.

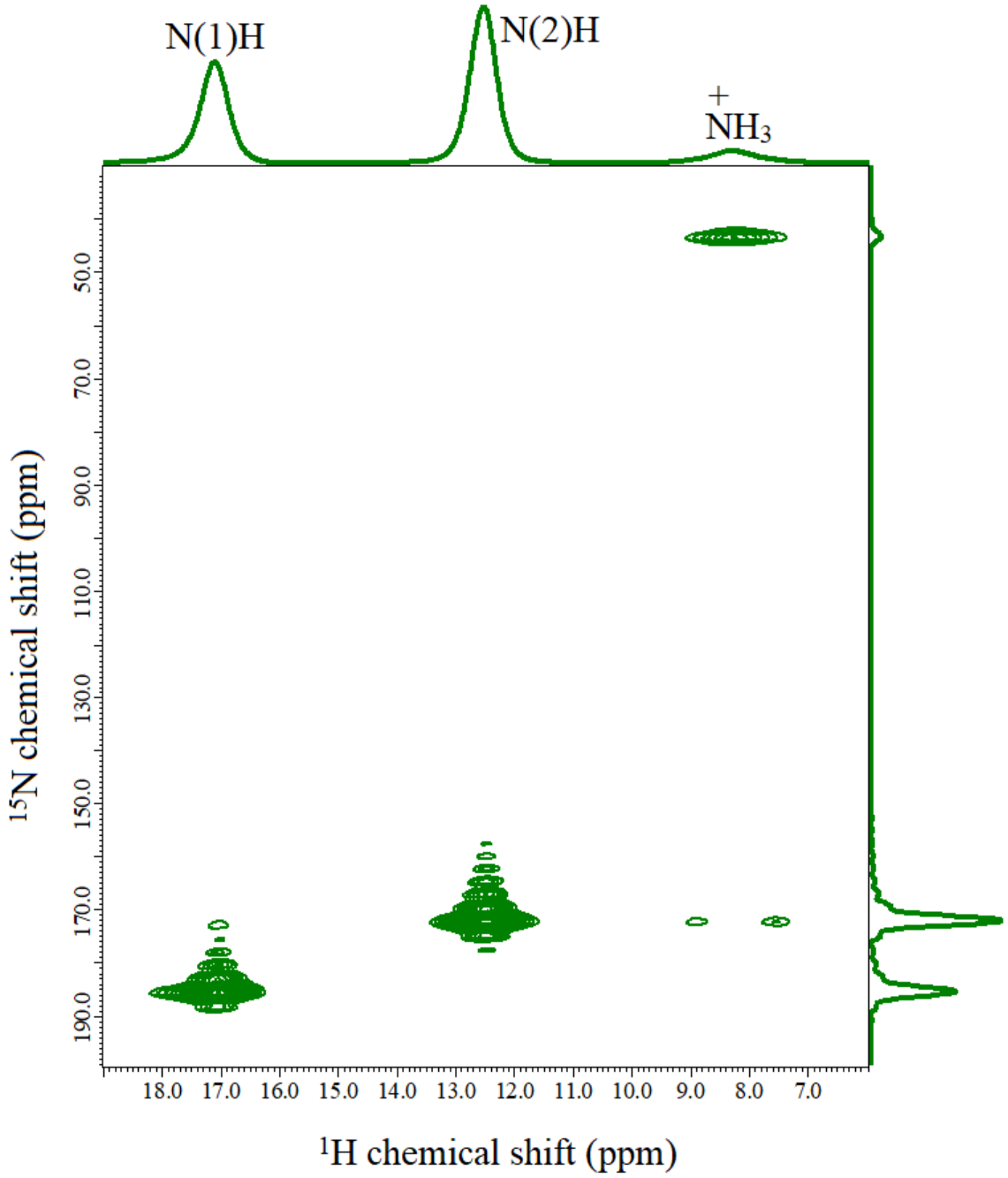

Figure S10: Proton-detected 2D ^{15}N CS/^{1}H CS correlation spectrum of U-^{15}N L-His.HCl.H_2O collected on a 600 MHz NMR spectrometer using the ^{1}H-^{15}N-^{1}H double cross-polarization (DCP) experiment under fast MAS rate of 69.832 kHz. Contact time used for the second CP transfer was 0.3 ms.

Details of the Quantum Chemical Calculations

Density Functional Theory (DFT) calculations on L-His.HCl.H2O (H. Fuess, et al., Acta Crystallogr. B33 (1977) 654–659) were performed using CASTEP module of Materials Studio 2019. Geometry optimization was performed before NMR parameter calculations using generalized gradient approximation (GGA) functional and the Perdew-Burke-Ernzerhof (PBE) exchange-correlation functional in an OTFG ultrasoft-pseudopotential formalism. The plane wave basis cut-off energy was set to 600 eV and geometry optimization tolerance levels were set to ultrafine. The chemical shift parameters were calculated for the optimized structure using gauge-including projector augmented-wave (GIPAW) method. NMR calculations were performed with plane wave basis cutoff energy of 700 eV and k-point spacing of 0.05 $Å^{-1}$. The following conventions were used

$$\sigma_{iso} = \frac{\sigma_{xx} + \sigma_{yy} + \sigma_{zz}}{3}$$

$$s_{ani} = s_{zz} - s_{iso}$$

$$\eta = \frac{\sigma_{yy} - \sigma_{xx}}{\sigma_{zz} - \sigma_{iso}}$$

$$\delta_{iso} = \sigma_{ref} - \sigma_{iso}$$

Reference value used for isotropic chemical shift referencing of ^1H (σ_{ref}) = 30.68 ppm.

Table S1: Comparison of experimental ^1H CSA parameters with the quantum chemical calculated values for the N(1)H and N(2)H groups of L-His.HCl.H_2O. The sign convention ($\delta_{ani} = - \sigma_{ani}$) used for the ^1H CSA is as per the reference J. Czernek and J. Brus, Molecules, 24 (2019) 1731.

1. **N(1)H**

δ_{iso} (ppm)		δ_{ani} (ppm)		η	
DFT	Experimental	DFT	Experimental	DFT	Experimental
18.6940	17.085	-17.9964	-15.3	0.2798	0.35

2. **N(2)H**

δ_{iso} (ppm)		δ_{ani} (ppm)		η	
DFT	Experimental	DFT	Experimental	DFT	Experimental
13.7570	12.5590	-9.7937	-7.8	0.6015	0.9

Proton-detected 3D ^{15}N-^{1}H DIP/^{1}H CSA/^{1}H CS pulse sequence

```
------------------------------------------------------------------------
-----------
--
--
--                          Experiment Source Code
--
--              Delta NMR Experiment & Machine Control Interface
--
--
--
--                     Copyright (c) 2005 JEOL Ltd
--
--                           All Rights Reserved
--
--
--
------------------------------------------------------------------------
-----------

header
    filename                    => "double_cp_dipshift_rocsa_3d"
    sample_id                   => "";
    comment                     => "double_cp_2d";
    process               => "1d_solid.list";
    include "header_solid";
end header;

instrument
    include "instrument_solid";
end instrument;

acquisition
        x_domain                =       "Proton";
        x_offset                =       5[ppm];
        x_sweep                         =       100[kHz];
        x_points                =       1024;
        scans                           =       8;
        x_prescans                      =       0;
        mod_return                      =       2;

        y_domain                =       x_domain;
        y_offset                =       0 [kHz];

        z_domain                =       x_domain;
        z_offset                =       0 [kHz];

        include "acquisition_solid";

end acquisition;

pulse
        collect COMPLEX,OBS REAL,OBS COMPLEX,OBS;
        initial_wait            =       10.0[ms];
```

```
irr_Setup                          =? "#Setup Irradiation#";
        irr_domain                          =>      "Nitrogen15",

help "decoupled nucleus";
        irr_offset                          =>      100[ppm],

        help "decoupler offset";

Pulse_Setup     =? "-----------Setup hard pulses-----------";

        obs_width_90     => x90;
        obs_amp_pulse    => 100[%];
        irr_width_90     => irr90;
        irr_width_180    => irr90 * 2;
        irr_amp_pulse    => 100[%];

        include "double_cp_solid";

symmetry_Setup   =? "-----------Setup symmetry-----------";

        obs_amp_symmetry          =>      100[%];
        symmetry_large_N          =>      3;
        symmetry_small_n          =       symmetry_large_N;
        symmetry_nu                               =       1;
        obs_phs_step                        =       360 *
symmetry_nu / symmetry_large_N;
        number_symmetry_y                   =>      1;
        y_points                            =>      16;
        number_symmetry_z                   =>      1;
        z_points                            =>      16;

        rocsa_a                                   => 0;
        rocsa_b                                   => 0.5;

        spinning_freq                       => 100 [kHz],
                                                        help
"spinning frequency";
        delay_rocsa1                        =       rocsa_a/
spinning_freq;
        delay_rocsa2                        =       (1/2-rocsa_a-
rocsa_b)/spinning_freq;
        obs_width_symmetry90      =       floor((1*rocsa_b/
(8*spinning_freq))/5[ns]+0.5)*5[ns];
        obs_width_symmetry360     =       4*obs_width_symmetry90;
        obs_width_symmetry270     =       3*obs_width_symmetry90;
        calc_spinning                       =?      1/
(16*obs_width_symmetry90);
        z_filter                            =>      1[ms];
        y_sweep                                     =>
calc_spinning/(symmetry_large_N*number_symmetry_y);
        z_sweep                                     =>
calc_spinning/(symmetry_large_N*number_symmetry_z);

MISC_Setup      =? "-----------Setup Miscellaneous-----------";
```

```
        include "obs_sat_solid";

        relaxation_delay => 5.0[s], help"inter-pulse delay";
        repetition_time          =?      relaxation_delay +
x_acq_time,                              help
"relaxation_delay+x_acq_time";

        include "obs_rdrfdr_solid";

        obs_atn                          =>      xatn,

help "attenuator of obs";
        irr_atn                          =>      irratn,

help "attenuator of irr";

        obs_phs_prep             =       {  0};
        obs_phs_cp1                      =       { 90};
        irr_phs_cp1                      =
{  0}.ystep(180%2);
        obs_phs_symmetry_y       =       {  0};
        obs_phs_dec                      =       {  0};
        irr_phs_180                      =       {2(  0),2( 90),
2(180),2(270)};
        irr_phs_store            =       { 90};

        obs_phs_rrx                      =       {  0};
        obs_phs_rry                      =       { 90};

        irr_phs_restore          =       {270};
        irr_phs_cp2                      =       {  0};
        obs_phs_cp2                      =       {{  0,180},
{ 90,270}}.zstep(180%2);
        obs_phs_symmetry_z       =       {  0};
        obs_phs_store            =       {8( 90),8(270)};
        obs_phs_restore  =       {16(0),16(120),16(240)};

        irr_phs_dec                      =       {  0};

        obs_phs_acq                      =       {2(  0,180,180,
0),2(180,  0,  0,180),

2(120,300,300,120),2(300,120,120,300),
                                                         2(240,
60, 60,240),2( 60,240,240, 60)}.ystep(180%2).zstep(180%2);

        include "pulse_solid";

        module_config = "solid_sample";

begin
    initial_wait;
```

```
        when SATURATION do
                obs_sat(sat_loop, sat_pulse_interval,
obs_width_sat, obs_amp_sat, obs_atn);
        end when;

        when RD_RFDR do
                obs_rdrfdr(number_rd_rfdr_m, relaxation_delay_rfdr,
number_rd_rfdr, tau_rdrfdr,
                obs_width_rd_rfdr, obs_phs_rd_rfdr,
obs_amp_rd_rfdr, obs_atn);
        end when;

        when NOT RD_RFDR do
                relaxation_delay;
        end when;

when MISSISSIPPI do
        on(spoil);
        pfg_width;
        off(spoil);
        delay_spoil;
end when;

        external_wait;
        1[us];
        obs_width_90, (obs.gate, obs.phs.obs_phs_prep,
obs.amp.obs_amp_pulse,   obs.atn.obs_atn);

        contact_time, (obs.GATE, obs.PHS.obs_phs_cp1, obs.shape.
{obs_shape_cp, "obs"}, obs.ATN.obs_atn,
                        irr.GATE, irr.PHS.irr_phs_cp1, irr.SHAPE.
{irr_shape_cp, "irr"}, irr.ATN.irr_atn);
loop ystep {0->512:1} times
loop number_symmetry_y times

        delay_rocsa1;
        obs_width_symmetry90,    (obs.gate,
obs.phs.obs_phs_symmetry_y,      obs.amp.obs_amp_symmetry,
obs.atn.obs_atn);
        obs_width_symmetry360,   (obs.gate,
obs.phs.obs_phs_symmetry_y+180,  obs.amp.obs_amp_symmetry,
obs.atn.obs_atn);
        obs_width_symmetry270,   (obs.gate,
obs.phs.obs_phs_symmetry_y,      obs.amp.obs_amp_symmetry,
obs.atn.obs_atn);
        delay_rocsa2;

        delay_rocsa2;
        obs_width_symmetry270,   (obs.gate,
obs.phs.obs_phs_symmetry_y,      obs.amp.obs_amp_symmetry,
obs.atn.obs_atn);
        obs_width_symmetry360,   (obs.gate,
obs.phs.obs_phs_symmetry_y+180,  obs.amp.obs_amp_symmetry,
obs.atn.obs_atn);
```

```
        obs_width_symmetry90,    (obs.gate,
obs.phs.obs_phs_symmetry_y,      obs.amp.obs_amp_symmetry,
obs.atn.obs_atn);
        delay_rocsa1;

        delay_rocsa1;
        obs_width_symmetry90,    (obs.gate,
obs.phs.obs_phs_symmetry_y+120,  obs.amp.obs_amp_symmetry,
obs.atn.obs_atn);
        obs_width_symmetry360,   (obs.gate,
obs.phs.obs_phs_symmetry_y+300,  obs.amp.obs_amp_symmetry,
obs.atn.obs_atn);
        obs_width_symmetry270,   (obs.gate,
obs.phs.obs_phs_symmetry_y+120,  obs.amp.obs_amp_symmetry,
obs.atn.obs_atn);
        delay_rocsa2;

        delay_rocsa2;
        obs_width_symmetry270,   (obs.gate,
obs.phs.obs_phs_symmetry_y+120,  obs.amp.obs_amp_symmetry,
obs.atn.obs_atn);
        obs_width_symmetry360,   (obs.gate,
obs.phs.obs_phs_symmetry_y+300,  obs.amp.obs_amp_symmetry,
obs.atn.obs_atn);
        obs_width_symmetry90,    (obs.gate,
obs.phs.obs_phs_symmetry_y+120,  obs.amp.obs_amp_symmetry,
obs.atn.obs_atn);
        delay_rocsa1;

        delay_rocsa1;
        obs_width_symmetry90,    (obs.gate,
obs.phs.obs_phs_symmetry_y+240,  obs.amp.obs_amp_symmetry,
obs.atn.obs_atn);
        obs_width_symmetry360,   (obs.gate,
obs.phs.obs_phs_symmetry_y+60,   obs.amp.obs_amp_symmetry,
obs.atn.obs_atn);
        obs_width_symmetry270,   (obs.gate,
obs.phs.obs_phs_symmetry_y+240,  obs.amp.obs_amp_symmetry,
obs.atn.obs_atn);
        delay_rocsa2;

        delay_rocsa2;
        obs_width_symmetry270,   (obs.gate,
obs.phs.obs_phs_symmetry_y+240,  obs.amp.obs_amp_symmetry,
obs.atn.obs_atn);
        obs_width_symmetry360,   (obs.gate,
obs.phs.obs_phs_symmetry_y+60,   obs.amp.obs_amp_symmetry,
obs.atn.obs_atn);
        obs_width_symmetry90,    (obs.gate,
obs.phs.obs_phs_symmetry_y+240,  obs.amp.obs_amp_symmetry,
obs.atn.obs_atn);
        delay_rocsa1;
end loop;
end loop;
```

```
        y_points*(1/
calc_spinning)*symmetry_small_n*number_symmetry_y ystep -(1/
calc_spinning)*symmetry_small_n*number_symmetry_y, (obs.GATE,
obs.PHS.obs_phs_dec, obs.AMP.obs_amp_dec, obs.ATN.obs_atn,
obs.NOISE.obs_noise);
parallel begin
        2/calc_spinning, (obs.GATE, obs.PHS.obs_phs_dec,
obs.AMP.obs_amp_dec, obs.ATN.obs_atn, obs.NOISE.obs_noise);
justify center
        irr_width_180,   (irr.gate,       irr.phs.irr_phs_180,
irr.amp.irr_amp_pulse,   irr.atn.irr_atn);
end parallel;
        y_points*(1/
calc_spinning)*symmetry_small_n*number_symmetry_y, (obs.GATE,
obs.PHS.obs_phs_dec, obs.AMP.obs_amp_dec, obs.ATN.obs_atn,
obs.NOISE.obs_noise);

        irr_width_90,    (irr.gate,       irr.phs.irr_phs_store,
irr.amp.irr_amp_pulse,   irr.atn.irr_atn);
when MISSISSIPPI do
        on(spoil);
        pfg_width;
        off(spoil);
        delay_spoil;
end when;

        tau_rr, (obs.gate,       obs.phs.obs_phs_rrx,
obs.amp.obs_amp_rr,      obs.atn.obs_atn);
        tau_rr, (obs.gate,       obs.phs.obs_phs_rry,
obs.amp.obs_amp_rr,      obs.atn.obs_atn);
        tau_rr, (obs.gate,       obs.phs.obs_phs_rrx,
obs.amp.obs_amp_rr,      obs.atn.obs_atn);
        tau_rr, (obs.gate,       obs.phs.obs_phs_rry,
obs.amp.obs_amp_rr,      obs.atn.obs_atn);

        external_wait;
        1[us];
        irr_width_90,    (irr.gate,       irr.phs.irr_phs_restore,
irr.amp.irr_amp_pulse,   irr.atn.irr_atn);

        contact_time2, (obs.GATE, obs.PHS.obs_phs_cp2, obs.shape.
{obs_shape_cp2, "obs"}, obs.ATN.obs_atn,
                        irr.GATE, irr.PHS.irr_phs_cp2, irr.SHAPE.
{irr_shape_cp2, "irr"}, irr.ATN.irr_atn);

parallel begin
loop zstep {0->512:1} times
loop number_symmetry_z times

        delay_rocsa1;
        obs_width_symmetry90,    (obs.gate,
obs.phs.obs_phs_symmetry_z,      obs.amp.obs_amp_symmetry,
obs.atn.obs_atn);
        obs_width_symmetry360,   (obs.gate,
```

```
obs.phs.obs_phs_symmetry_z+180,   obs.amp.obs_amp_symmetry,
obs.atn.obs_atn);
        obs_width_symmetry270,    (obs.gate,
obs.phs.obs_phs_symmetry_z,       obs.amp.obs_amp_symmetry,
obs.atn.obs_atn);
        delay_rocsa2;

        delay_rocsa2;
        obs_width_symmetry270,    (obs.gate,
obs.phs.obs_phs_symmetry_z,       obs.amp.obs_amp_symmetry,
obs.atn.obs_atn);
        obs_width_symmetry360,    (obs.gate,
obs.phs.obs_phs_symmetry_z+180,   obs.amp.obs_amp_symmetry,
obs.atn.obs_atn);
        obs_width_symmetry90,     (obs.gate,
obs.phs.obs_phs_symmetry_z,       obs.amp.obs_amp_symmetry,
obs.atn.obs_atn);
        delay_rocsa1;


        delay_rocsa1;
        obs_width_symmetry90,     (obs.gate,
obs.phs.obs_phs_symmetry_z+120,   obs.amp.obs_amp_symmetry,
obs.atn.obs_atn);
        obs_width_symmetry360,    (obs.gate,
obs.phs.obs_phs_symmetry_z+300,   obs.amp.obs_amp_symmetry,
obs.atn.obs_atn);
        obs_width_symmetry270,    (obs.gate,
obs.phs.obs_phs_symmetry_z+120,   obs.amp.obs_amp_symmetry,
obs.atn.obs_atn);
        delay_rocsa2;

        delay_rocsa2;
        obs_width_symmetry270,    (obs.gate,
obs.phs.obs_phs_symmetry_z+120,   obs.amp.obs_amp_symmetry,
obs.atn.obs_atn);
        obs_width_symmetry360,    (obs.gate,
obs.phs.obs_phs_symmetry_z+300,   obs.amp.obs_amp_symmetry,
obs.atn.obs_atn);
        obs_width_symmetry90,     (obs.gate,
obs.phs.obs_phs_symmetry_z+120,   obs.amp.obs_amp_symmetry,
obs.atn.obs_atn);
        delay_rocsa1;


        delay_rocsa1;
        obs_width_symmetry90,     (obs.gate,
obs.phs.obs_phs_symmetry_z+240,   obs.amp.obs_amp_symmetry,
obs.atn.obs_atn);
        obs_width_symmetry360,    (obs.gate,
obs.phs.obs_phs_symmetry_z+60,    obs.amp.obs_amp_symmetry,
obs.atn.obs_atn);
        obs_width_symmetry270,    (obs.gate,
obs.phs.obs_phs_symmetry_z+240,   obs.amp.obs_amp_symmetry,
```

```
obs.atn.obs_atn);
        delay_rocsa2;

        delay_rocsa2;
        obs_width_symmetry270,    (obs.gate,
obs.phs.obs_phs_symmetry_z+240,   obs.amp.obs_amp_symmetry,
obs.atn.obs_atn);
        obs_width_symmetry360,    (obs.gate,
obs.phs.obs_phs_symmetry_z+60,    obs.amp.obs_amp_symmetry,
obs.atn.obs_atn);
        obs_width_symmetry90,     (obs.gate,
obs.phs.obs_phs_symmetry_z+240,   obs.amp.obs_amp_symmetry,
obs.atn.obs_atn);
        delay_rocsa1;

end loop;
end loop;
justify center
        irr_width_180,                    (irr.gate,
irr.phs.irr_phs_dec,     irr.amp.irr_amp_pulse, irr.atn.irr_atn);
end parallel;

        obs_width_90,             (obs.gate,
obs.phs.obs_phs_store,            obs.amp.obs_amp_pulse,
obs.atn.obs_atn);
        z_filter;
        obs_width_90,             (obs.gate,
obs.phs.obs_phs_restore,          obs.amp.obs_amp_pulse,
obs.atn.obs_atn);

        on(irr.GATE, irr.PHS.irr_phs_dec, irr.AMP.irr_amp_dec,
irr.ATN.irr_atn, irr.NOISE.irr_noise);
        acq( dead_time, delay, obs_phs_acq );
        off(irr.GATE, irr.PHS.irr_phs_dec, irr.AMP.irr_amp_dec,
irr.ATN.irr_atn, irr.NOISE.irr_noise);

end pulse;
```

SIMPSON input for the 2D ^{1}H CSA/^{15}N-^{1}H dipolar coupling correlations

```
spinsys {
channels 1H 15N
nuclei   1H 15N

         shift 1 0.0p -8.3p 0.8 0 0 0
         dipole 1 2 10800 0 70 0
}

par {
         spin_rate                69832
         proton_frequency 600e6
         gamma_angles     60
         crystal_file     rep168
         np                                16
         ni                                32
         start_operator   I2x
         detect_operator  I1p
         method                   direct
         verbose                  1101
         conjugate_fid    true
         variable rocsa_a 0.0
         variable rocsa_b 0.5
         variable symmetry_n 3
    variable        number_symmetry 2
         variable rf_scale 1
    variable        rfdec     10000
    variable     ct               286.401649
         variable cp_15N          50000
    variable     cp_1H            spin_rate-50000
    sw           spin_rate/(number_symmetry * symmetry_n)
         sw1              sw


}

proc pulseq {} {
global par
maxdt 0.1

         set tr [expr (1e6 / $par(spin_rate))]
        set tau [expr
(12e6/$par(spin_rate))*$par(number_symmetry)*$par(symmetry_n)]
         set pw90 [expr $par(rocsa_b)*$tr/8]
         set pw360 [expr $pw90*4]
         set pw270 [expr $pw90*3]
         set rf [expr $par(rf_scale) * 1e6 / $pw360]



reset
```

```
#turnoff dipole_1_2
turnoff shift_1
#turnoff shift_2
        for { set i 0} {$i < $par(symmetry_n)} { incr i } {
        delay [expr $par(rocsa_a)*$tr]
        pulse $pw90 $rf  [expr 360 * $i / $par(symmetry_n)] 0 0
        pulse $pw360 $rf [expr 360 * $i / $par(symmetry_n) + 180] 0
0
        pulse $pw270 $rf [expr 360 * $i / $par(symmetry_n)] 0 0
        delay [expr $tr*(0.5 - $par(rocsa_a) - $par(rocsa_b))]

        delay [expr $tr*(0.5 - $par(rocsa_a) - $par(rocsa_b))]
        pulse $pw270 $rf  [expr 360 * $i / $par(symmetry_n)] 0 0
        pulse $pw360 $rf [expr 360 * $i / $par(symmetry_n) + 180] 0
0
        pulse $pw90 $rf [expr 360 * $i / $par(symmetry_n)] 0 0
        delay [expr $par(rocsa_a)*$tr]

        delay [expr $par(rocsa_a)*$tr]
        pulse $pw90 $rf  [expr 360 * $i / $par(symmetry_n)] 0 0
        pulse $pw360 $rf [expr 360 * $i / $par(symmetry_n) + 180] 0
0
        pulse $pw270 $rf [expr 360 * $i / $par(symmetry_n)] 0 0
        delay [expr $tr*(0.5 - $par(rocsa_a) - $par(rocsa_b))]

        delay [expr $tr*(0.5 - $par(rocsa_a) - $par(rocsa_b))]
        pulse $pw270 $rf  [expr 360 * $i / $par(symmetry_n)] 0 0
        pulse $pw360 $rf [expr 360 * $i / $par(symmetry_n) + 180] 0
0
        pulse $pw90 $rf [expr 360 * $i / $par(symmetry_n)] 0 0
        delay [expr $par(rocsa_a)*$tr]

}
#turnon dipole_1_2
turnon shift_1
#turnon shift_2

store 1

reset
turnoff dipole_1_2
        for { set i 0} {$i < $par(symmetry_n)} { incr i } {
        delay [expr $par(rocsa_a)*$tr]
        pulse $pw90 $rf  [expr 360 * $i / $par(symmetry_n)] 0 0
        pulse $pw360 $rf [expr 360 * $i / $par(symmetry_n) + 180] 0
0
        pulse $pw270 $rf [expr 360 * $i / $par(symmetry_n)] 0 0
        delay [expr $tr*(0.5 - $par(rocsa_a) - $par(rocsa_b))]

        delay [expr $tr*(0.5 - $par(rocsa_a) - $par(rocsa_b))]
        pulse $pw270 $rf  [expr 360 * $i / $par(symmetry_n)] 0 0
        pulse $pw360 $rf [expr 360 * $i / $par(symmetry_n) + 180] 0
0
        pulse $pw90 $rf [expr 360 * $i / $par(symmetry_n)] 0 0
```

```
        delay [expr $par(rocsa_a)*$tr]

        delay [expr $par(rocsa_a)*$tr]
        pulse $pw90 $rf  [expr 360 * $i / $par(symmetry_n)] 0 0
        pulse $pw360 $rf [expr 360 * $i / $par(symmetry_n) + 180] 0
0
        pulse $pw270 $rf [expr 360 * $i / $par(symmetry_n)] 0 0
        delay [expr $tr*(0.5 - $par(rocsa_a) - $par(rocsa_b))]

        delay [expr $tr*(0.5 - $par(rocsa_a) - $par(rocsa_b))]
        pulse $pw270 $rf  [expr 360 * $i / $par(symmetry_n)] 0 0
        pulse $pw360 $rf [expr 360 * $i / $par(symmetry_n) + 180] 0
0
        pulse $pw90 $rf [expr 360 * $i / $par(symmetry_n)] 0 0
        delay [expr $par(rocsa_a)*$tr]
}
turnon dipole_1_2
store 2
reset
store 10

for {set t1 1} {$t1 < [expr $par(ni)/2]} {incr t1} {

        reset
        if      {$t1 > 1} {
                prop 3
                prop 1
                }
        store 3

    set tdec [expr $tau-$tr*($t1-1.0)]
    pulse $tdec $par(rfdec) 0 0 0
        pulseid 5 0 0 100000 0
       pulse $tau $par(rfdec) 0 0 0
        pulse $par(ct) $par(cp_1H) 0 $par(cp_15N) 0
        acq $par(np) 2
        reset
        acq $par(np) 10
        }
}


proc main {} {
        global par
   for {set par(gamma) 0} {$par(gamma) <= 180} {incr par(gamma) 10}
{
   set f [fsimpson [list [list dipole_1_2_gamma $par(gamma)]]]
   fsave $f $par(name)_[expr $par(gamma)].fid
   funload $f
}
}
```

Highlights

- Proton-detected 3D ^{15}N-^{1}H dipolar coupling/^{1}H CSA/^{1}H CS pulse sequence is developed at fast MAS
- Relative orientation between the ^{15}N-^{1}H dipolar coupling and ^{1}H CSA tensors is measured
- Windowless C-symmetry based ROCSA-DIPSHIFT is integrated with ROCSA for the recoupling of the ^{15}N-^{1}H dipolar coupling and ^{1}H CSA tensors, respectively
- The 2D ^{15}N-^{1}H dipolar coupling/^{1}H CSA powder pattern is sensitive to the sign and asymmetry of the ^{1}H CSA, and exhibits profound dependence on the dipolar PAS angles

TOC

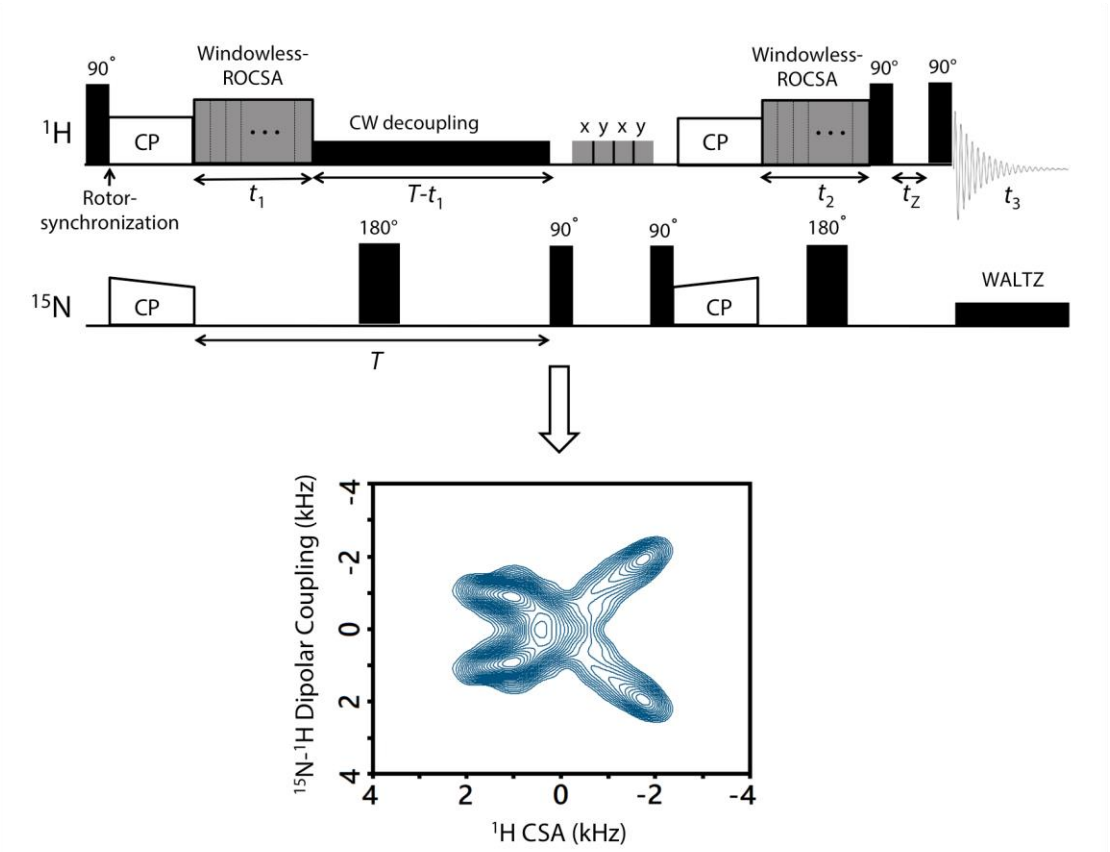
90°
Windowless-ROCSA
CW decoupling
x y x y
Windowless-ROCSA
90°
90°
^{1}H
CP
CP
Rotor-synchronization
t_1
T-t_1
t_2
t_Z
t_3
180°
90°
90°
180°
^{15}N
CP
CP
WALTZ
T
^{15}N-^{1}H Dipolar Coupling (kHz)
4
2
0
-2
-4
^{1}H CSA (kHz)